Aerospace Science and Technology 113 (2021) 106645

Contents lists available at ScienceDirect

Aerospace Science and Technology

www.elsevier.com/locate/aescte

UAV airborne collision to manned aircraft engine: Damage of fan blades and resultant thrust loss

Hu Liu [b], Mohd Hasrizam Che Man [b], Kin Huat Low [a,*]

[a] School of Mechanical and Aerospace Engineering, Nanyang Technological University, 639798, Singapore
[b] Air Traffic Management Research Institute, Nanyang Technological University, 637460, Singapore

ARTICLE INFO

Article history:
Received 13 September 2020
Received in revised form 26 January 2021
Accepted 9 March 2021
Available online 6 April 2021
Communicated by Zhao Dan

Keywords:
UAV airborne collision
Engine ingestion
Bird strike
Thrust loss
Risk assessment
Drone collision

ABSTRACT

Recently, the growing amount of unmanned aerial vehicles (UAVs) has brought a huge threat to the safety management of manned aircraft operation, in which the UAV airborne collision is an incident that would lead to serious damage to the manned aircraft and will affect its operational safety significantly. In the present paper, the bird strike data over the year of 1990∼2019 is analyzed, which demonstrates that the engine is the most vulnerable component under bird strike, and the most severe hazard would happen during the flight phases of take-off, climb and approach. The dynamic response of UAV airborne collision with the manned aircraft engine is simulated based on the combination of FEM (Finite Element Method) and CFD (Computational Fluid Dynamics) simulations. Not only the damage of fan blades but also the thrust loss of the engine core caused by the damage in the compressor core is taken into account. The damage severity level of the engine under UAV airborne collision is studied by considering different collision configurations, different collision positions and different flight phases. Both the damage of fan blades and the percentage of thrust loss are considered to reflect the influence of UAV airborne collision on the aircraft operation. It is expected that this study can be used to guide the airborne safety assessment of UAV airborne collision.

1. Introduction

Recently, the application of unmanned aerial vehicles (UAVs) has been getting more and more popular in the fields of airspace surveillance, target tracking, and aerial mapping [1–3]. It is estimated that the number of UAVs over the world will reach 4.7 million unities by the year 2020 [4], which would lead to great threats for the safety management of manned aircraft operation [5]. Based on the data of UAV involving incidents given in Ref. [6], a statistics of the number of UAV involving incidents over the past ten years is presented in Fig. 1, which shows that the UAV involving incidents increase significantly since the year of 2016 due to the increasing applications of UAVs. Once a UAV intrudes on the restricted airspace over the airport, the airport runway should be closed to avoid the collision chance between the UAV and manned aircraft [7]. As an important safety issue, the potential damage of manned aircraft caused by the UAV airborne collision should be investigated carefully.

1.1. Existing works

Focusing on this problem, many experimental and simulation works have been conducted to assess the collision severity of manned aircraft struck by UAVs. For instance, Olivares et al. [8,9] performed the pioneering studies to analyze the UAS airborne collision severity level of different components of commercial aircraft subjected to the striking by quadrotor and fixed-wing UAVs. A series of outdoor experiments of UAVs impacting onto a windscreen of commercial aircraft were carried out by Lu et al. [10] to reveal the influence of pitch and yaw angles of UAVs on the damage of windscreen. Additionally, the experimental and simulation studies on the UAS airborne collision to the horizontal stabilizer were also carried out to evaluate the damage severity caused by the UAV impinging [11]. From these researches, it is concluded that UAV impacts are likely associated with higher damage levels than bird strikes for an equivalent initial kinetic energy due to the hard-bodied construction of the UAVs with their components composed of dense and rigid materials.

* Corresponding author.
E-mail address: mkhlow@ntu.edu.sg (K.H. Low).

https://doi.org/10.1016/j.ast.2021.106645
1270-9638/

Nomenclature of abbreviations and symbols

UAV	Unmanned aerial vehicle
FEM	Finite element method
CFD	Computational fluid dynamics
LPC	Low-pressure compressor
HPC	High-pressure compressor
IGV	Inlet Guide Vane
FOD	Foreign Object Debris
r_{P_ENG}	Engine pressure ratio
P_{in}	Input pressure of the engine
P_{out}	Output pressure of the engine
P_{in_i}	Input pressure of ith ($i = IGV, 1, \dots, N$) stage
P_{out_i}	Output pressure of ith ($i = IGV, 1, \dots, N$) stage
r_{P_i}	Pressure ratio of ith ($i = IGV, 1, \dots, N$) stage
r_{P_IGV}	Pressure ratio of IGV stage
$r_{P\_i\_damage}$	Pressure ratio in ith ($i = IGV, 1, \dots, N$) damaged stage
$r_{P\_1\_damage}$	Pressure ratio in damaged stage-1 LPC
$r_{P\_ENG\_damage}$	Engine pressure ratio with considering the damage of engine core
$r_{P\_ENG\_no}$	Engine pressure ratio with no damage of engine core
$P_{out\_1\_damage}$	Output pressure damaged stage-1 LPC
$P_{in\_1\_damage}$	Input pressure damaged stage-1 LPC
r_{P_other}	Engine pressure ratio without considering ith ($i = IGV, 1, \dots, N$) stage
$\dot{m}$	Mass flow rate at the exhaust of the engine
V	Mass flow velocity at the exhaust of the engine
A	Area of engine inlet
T	Engine thrust
ΔT	Thrust loss of engine
D	Depth of the damage of fan blades
W	Width of the damage of fan blades
θ	Drop angle of UAV adopted in the drop test simulation

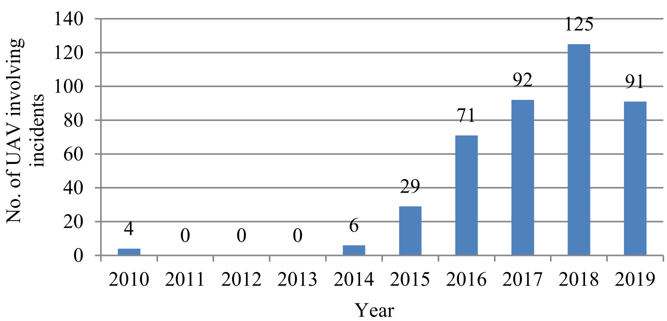

Fig. 1. Number of UAV involving incidents over the past ten years [6].

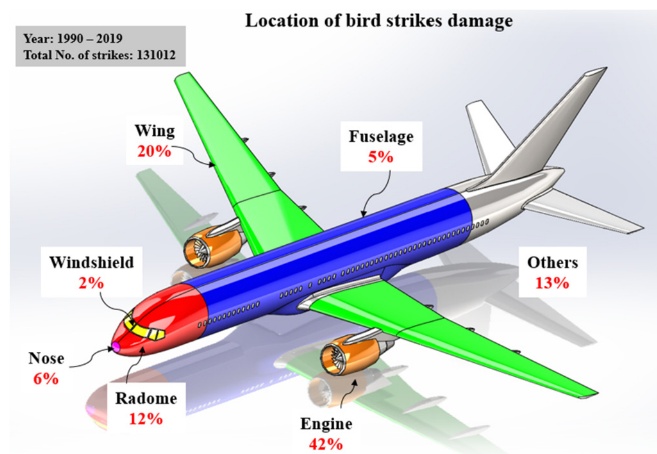

Fig. 2. Damage percentage of different components under bird strike.

Particularly, the damage of the manned aircraft engine induced by the UAV ingestion has aroused wide attention. For instance, the damages of the fan blades, containment ring, and nose cone of manned aircraft engines caused by the UAV ingestion were investigated by D'Souza et al. [12], in which influences of collision position and postures on the damage of manned aircraft engine were analyzed in detail. The damage of engine fan blades under the bird and UAV strikes was compared by Bayandor et al. [13,14] and they demonstrated that the UAV strike would result in much more severe damage compared to the bird strike. A similar conclusion also has been demonstrated by Lyons and D'Souza [15]. However, there are also some limitations in their studies, e.g., a non-specific engine model in service was employed in D'Souza et al.'s works [12,15], and only a simplified drone model is used in Bayandor et al.'s studies [13,14]. In our previous study [16], a UAV impacting onto a specific engine (CFM-56-5B) was analyzed to investigate the damage of fan blades under different UAV collision positions and postures. However, a significant drawback of all these works is that only the damage of engine fan blade is taken into account, while the potential damage of engine core due to the ingested debris is not analyzed. Furthermore, the resultant thrust loss of engine due to the UAV ingestion also has not been revealed in all previous studies.

Due to the limited information of UAV strike incidents, the studies on the UAV airborne collision incidents are still very limited by comparing with those of bird strikes which have been reported extensively in the last decades. Because the bird strike and drone collision are both happened suddenly and unpredictably, the statistical analysis of the data of bird strikes might be useful as a start point to explore the damage severity assessment of UAV airborne collision.

1.2. Relevant statistics of bird strike damage

As is known to all, the bird strike is an airborne collision between a flying bird and a manned aircraft, which is a major threat to the safety of civil aviation as this incident can lead to serious structural damage [17–22]. According to the Federal Aviation Administration (FAA), it was reported that more than 258 people had been killed and at least 245 aircraft have been destroyed under the bird strike accidents during the year of 1988-2014 [23]. The bird strike performances of the wing leading edge [24,25], wing flap [26,27], engine [28], and windshield [29,30] were extensively investigated by several researchers.

By learning from bird strike, a total number of 131,032 bird strike incidents during the period 1990-2019 was collected [31]. From these data, the damage percentage caused by the bird strike on different components of aircraft can be obtained, as presented in Fig. 2. It is found that the engine part is more susceptible to be damaged under bird strikes by comparing to the other manned aircraft parts. As is known to all, the engine part is the sole component to provide the power and thrust to the whole manned aircraft; hence, the failure of this part may cause loss control of aircraft and eventually lead to catastrophic accidents. As the most critical component in the commercial aircraft, the engine ingestion of UAVs will be focused in the present work.

Next, the data analysis on the bird ingestion incidents was performed to detect which type of engine is the most used one. From

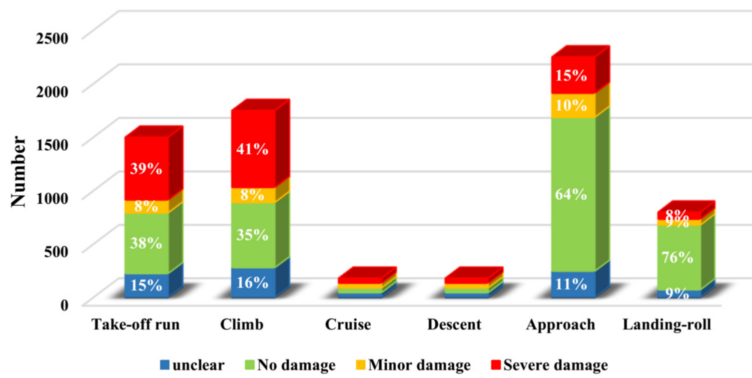

Fig. 3. Damage level of bird ingestion incidents under different flight phases. (For interpretation of the colors in the figure(s), the reader is referred to the web version of this article.)

the database sweep study done, it was found that CFM56, P&W, and GE are the top three engine types involving an airborne collision incident with the bird. Hence, the concentration will be paid on the simulation of UAV collision on the CFM56-5B engine in the following sections. In addition, the data of bird ingestion incidents are detailed analyzed to estimate the severity level under different flight phases, as presented in Fig. 3. It is found that most bird strike incidents appear during the approach, climb, take-off, and landing flight phases. Besides, the most severe damage often happens during climb and take-off flight phases, whose rates can reach 41% and 39%, respectively. The proportion of severe damage cases under the approach phase is about 15%, which also poses a significant hazard to the aircraft engine. Hence, a significant concern will be paid to the climb, take-off, and approach flight phases in the following studies.

1.3. Bird strike to engine

Due to the high chance of severe damage accidents under bird ingestion, the problem of birds strike on an aircraft engine requires careful investigation. Hence, the literature review on experiment and simulation studies of bird ingestion is carried out to provide a preliminary understanding of the dynamic response of aircraft engine under striking load. For the simulation study of bird ingestion, Meguid et al. [32] classified the bird into three different geometry configurations (i.e., straight and hemispherical-ended cylinders, as well as an ellipsoid) and investigated the impacting response of a single fan blade subjected to bird strike by using the finite element method (FEM). Vignjevic et al. [33] treated the bird as Smoothed Particle Hydrodynamics (SPH) particles and analyzed the influence of bird shape, bird impact location, and impact timing on the deformed shape of the fan blade. With the aid of the same simulation method, Zhang and Fei [34] detected the influence of bird geometry and impact orientation on the bird striking onto a rotating jet-engine fan blades. Zhang et al. [28] analyzed the influences of arbitrary yaw/pitch angle on the bird-striking response of a rotary jet-engine fan blades. For the experimental study of bird ingestion, Liu et al. [35] built a real bird-striking experimental system by launching the bird onto the rotary engine blades to assess the dynamic damage of the engine blade. A numerical analysis model based on the SPH method was also established to investigate the influence of bird speed, mass, rotating speed, and impact location on the dynamic deformation process of the engine blades. A similar study was also performed by Hou et al. [36] to evaluate the damage of a rotary engine fan assembly with hollow blades subjected to bird strikes.

It is noted that the engine fan blades mentioned above are mostly made of titanium alloy Ti-6Al-4V, and there are also some works on rotating composite engine blades subjected to the bird strike. For instance, Zhou et al. [37] numerically simulated the damage of rotating laminates induced by the bird strike based on the SPH-FEM approach. The same method is also adopted by Zhou et al. [38] to analyze the deformation and stress responses of a simplified slender composite blade impacted by the bird projectile. Moreover, the experimental study for the bird strike on a simplified composite blade-like plate was carried out by Liu et al. [39] to evaluate the damage level of the composite engine blade caused by a bird strike.

Besides, there are also some bird ingestion certifications that have focused on the thrust loss of engine led by the bird ingestion. For example, in the engine certification for the ingestion of a single bird with a maximum weight of 1.35 kg, it is required that the bird strike should not cause a sustained thrust or power loss of more than 25% and shall not result in hazardous engine conditions [40]. For engine ingestion test of large bird (weight between 1.85 kg and 3.65 kg) certification regulation, it is required the aircraft engine shall enable to maintain at least 50% thrust after a large bird impact, and this must be proved for the entire engine certification test [41]. Besides, it also has to be proven that the engine inlet can withstand a large bird impact with no damage to significant components of the engine [41]. However, most previous evaluations are solely dependent on experiments, and no simulation results on thrust loss have been reported.

1.4. Contribution of this paper

From the above literature review, although many works have been performed to evaluate the damage of bird strike on the aircraft engine, most of them are only focused on the damage of the engine fan blades. There are two main problems remained to be solved:

a) The UAV debris may be ingested into the engine compressor core and cause damage to the engine compressor blades, which has not been studied in previous works. By comparing it with the bird strike, the UAV debris would lead to much more serious damage to the engine compressor blades due to its higher density and rigidity.
b) Although the damage of the fan blades has been studied by many researchers, the consequences of a UAV collision on commercial aircraft, especially on the thrust loss of aircraft engine are still unclear.

Facing these two problems for the UAV airborne collision to the manned aircraft engine, the following methods will be carried out:

a) For the first problem, by adopting the collision simulation of the UAV impinging on the engine fan blades, the damage of the fan blades can be analyzed. Moreover, the collision simulation will be continued to see the damage of the compressor blades induced by the UAV debris ingested into the engine compressor core. From these simulation studies, the damage of the fan blades and compressor blades both can be obtained.

b) To solve the second problem, the operational effect caused by UAV ingestion is analyzed by combining the damage of the fan blades with the thrust loss of the compressor core. The pressure ratio in the compressor can be analyzed by using CFD (Computational Fluid Dynamics) simulation, and the failed compressor blades will lead to the reduction of pressure ratio in the compressor, which can be used to define the thrust loss of the aircraft engine.

The outline of this paper is presented as follows: in the introduction part, a data study on the bird strike was performed to exhibit the most critical engine type and flight phases. Next, the methodology adopted in this paper will be discussed in detail in Section 2. The simulation on the UAV airborne collision on the aircraft engine is carried out by combining FEM with CFD, which are explained in detail in Section 3. Then, the validation of the UAV and engine models is presented in Section 4. In the next section, several numerical simulations are performed to determine the damage severity of the engine impinged at different collision configurations and positions under the take-off, climb, and approach flight phases. Finally, several conclusions are drawn in Section 6.

2. Methodology of analysis

To assess the damage severity of the UAV airborne collision, a two-stage simulation approach will be employed. In the first stage, the damage of fan blades and engine core (including a low-pressure compressor (LPC) and high-pressure compressor (HPC)) caused by UAV airborne collision will be studied. In the next stage, the thrust loss of engine cone resulted by the engine core damage will be estimated.

2.1. Engine damage assessment

The region to be considered in our study is highlighted in Fig. 4, in which the region of fan blades and engine core (including LPC and HPC blades) will be taken into account. The first stage is carried out by FEM to check the damage of UAV airborne collision damage of fan blades, LPC and HPC blades. Subsequently, in the secondary stage, the thrust loss caused by the damage of engine core blades will be estimated by using the reduction of pressure ratio obtained via CFD simulation.

As shown in Fig. 5, the UAV-engine assembly system for UAV ingestion simulation is presented, in which the UAV will impact the rotating engine with an initial velocity (the relative velocity between UAV and engine). Moreover, accurate material properties and boundary conditions will also be provided for the UAV-engine system. After the UAV ingestion simulation, the damage of fan blades, LPC and HPC blades can be examined. The detailed models for the UAV and engine will be explained in Section 3.

2.2. Thrust loss estimation

In this subsection, the estimation method for the thrust loss of the engine core is explained. A diagram for the engine core with IGV (Inlet Guide Vane), LPC, and HPC is presented in Fig. 4. The engine pressure ratio (r_{P_ENG}) can be achieved by using the output pressure dividing the input one [43]

$$r_{P\_ENG} = P_{out}/P_{in} \tag{1}$$

in which P_{in} and P_{out} denote the input and output pressures of the engine, respectively. Similarly, the pressure ratio in each stage also can be derived by using the behind pressure P_{out_i} dividing the front one P_{in_i}, i.e.,

$$r_{P\_i} = P_{out\_i}/P_{in\_i} \tag{2}$$

in which ith ($i = IGV, 1, \dots, N$) denotes the stage number of the engine core, wherein the subscript IGV denotes the IGV stage, and N is the total number of stages in the engine core. Then, the engine pressure ratio of the engine can be re-calculated by

$$r_{P\_ENG} = r_{P\_IGV} \prod_{i=1}^{N} r_{P\_i} \tag{3}$$

Once the blade in one stage is damaged, one can get the pressure ratio in this damaged stage $r_{P\_i\_damage}$. Take the damage of stage-1 LPC as an example, the engine pressure ratio $r_{P\_ENG\_damage}$ with considering the damage of this stage can be re-evaluated as

$$\begin{aligned} r_{P\_ENG\_damage} &= P_{out\_damage}/P_{in} = (P_{in} r_{P\_1\_damage} r_{P\_other})/P_{in} \\ &= r_{P\_1\_damage} r_{P\_other} \end{aligned} \tag{4}$$

in which $r_{P\_1\_damage}$ can be calculated by using the behind pressure $P_{out\_1\_damage}$ of the damaged stage-1 LPC dividing the front pressure $P_{in\_1\_damage}$, and r_{P_other} is the pressure ratio of other stages, which satisfies,

$$r_{P\_other} = r_{P\_IGV} \prod_{j=2}^{N} r_{P\_j} \quad (j = 2, \dots, N) \tag{5}$$

Here, the pressure $P_{out\_1\_damage}$ can be obtained by using CFD simulation.

The engine thrust (T) provided by the engine core is a key index to monitor the state of commercial aircraft operation, and this engine thrust can be qualified by using the input and output pressures, i.e., [44]

$$T = \dot{m}V + A(P_{out} - P_{in}) = \dot{m}V + A(r_{P\_ENG} - 1)P_{in} \tag{6}$$

in which $\dot{m}$ and V are the mass flow rate and velocity at the exhaust of the engine, respectively; A stands for the area of engine inlet.

The total thrust loss can be obtained by considering the drop of engine pressure ratio caused by engine core damage $r_{P\_ENG\_damage}$ led by different stages together. Finally, the thrust loss of engine (ΔT) also can be derived by

$$\Delta T = (r_{P\_ENG\_no} - r_{P\_ENG\_damage})/r_{P\_ENG\_no} \times 100\% \tag{7}$$

in which $r_{P\_ENG\_damage}$ denotes the engine pressure ratio without engine core damage. The goal of our CFD simulation is to evaluate the drop of engine pressure ratio caused by engine core damage $r_{P\_ENG\_damage}$.

To exhibit the process of thrust loss estimation much more clearly, a flow chart is given, as shown in Fig. 6. Firstly, the damage of each stage of the engine core will be checked based on the UAV collision simulation via FEM. If this stage is not damaged, the engine pressure in this stage remains the same as the undamaged engine, which can be obtained by the engine pressure data [45]. If one stage is damaged, an equivalent CAD model (shown in Section 3.2) will be established to obtain the engine pressure in this damaged stage. Finally, the total engine pressure and the corresponding thrust loss can be evaluated.

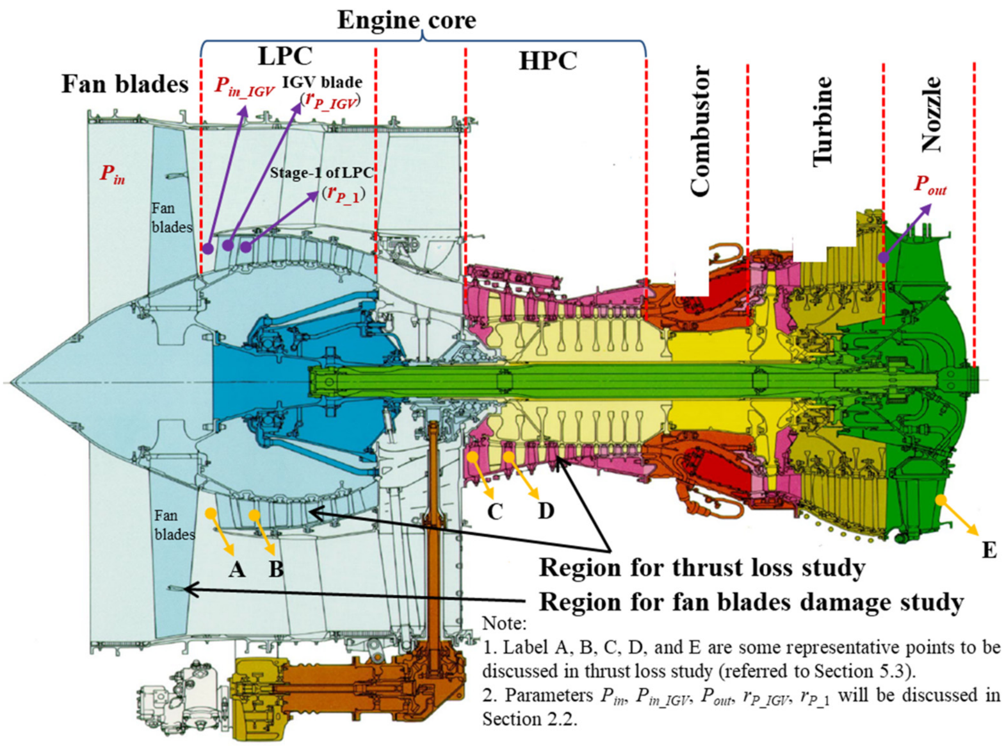

Fig. 4. Regions of fan blades, LPC, and HPC considered in this study (Modified from Ref. [42]).

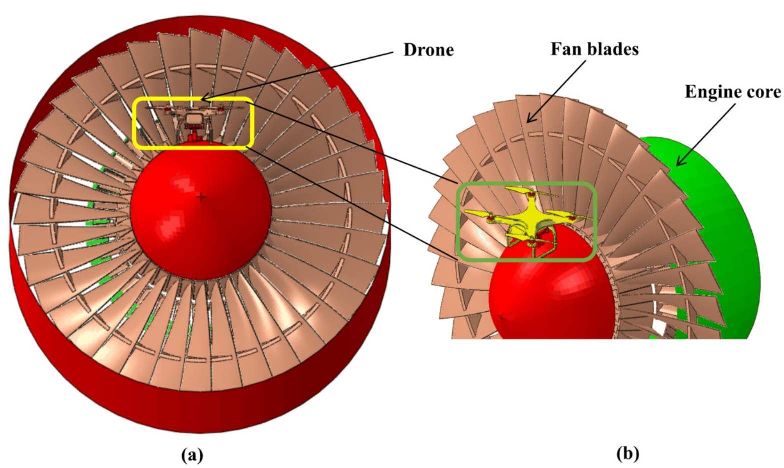

Fig. 5. UAV-engine assembly system for UAV ingestion simulation: (a) front view; (b) isometric view.

2.3. Simulation scenarios and parameters

In our study, the influence of flight phase, collision configuration and position both will be analyzed. Here, three flight phases including take-off, climb, and approach flight phases are considered, in which the aircraft velocity, engine rotation speed, and inclination angle of the engine for different flight phases are different. In the UAV airborne collision study, the relative velocity between the manned aircraft engine and the UAV is an important parameter which may affect the severity level significantly. As pointed out in Ref. [12], the operational velocity of manned aircraft can be approximated as the relative velocity in the simulation study because the operational speed of UAVs is much smaller than that of the manned aircraft engine. The parameters for these three different phases that will be considered in the present work are listed in Table 1. Besides, in most cases, the UAV is flying horizontally, while the manned aircraft flies with different angles under different flight phases. Hence, the horizontally moving UAV impacting onto the engine with inclination/declination angles is considered in this work. The largest flight angles which may lead to more serious damage on aircraft engine are selected, i.e., 10°, 18°, −10° are taken into account for the take-off, climb, and approach flight phases, respectively, as depicted in Table 2. Due to the flight angle of the aircraft, one has two collision configurations (i.e., positions above and below the nose cone) for each flight phase.

In addition, the influence of the collision position on the damage of the engine is also examined. The collision position can be defined by using the percentage along the fan blade, in which 0% position denotes the root of the fan blade, while a 100% position stands for the tip of the fan blade. To capture the worst cases under the airborne drone collision, three collision position cases including 12.5%, 25%, and 75% positions are considered, in which more debris may be ingested into the engine core for the

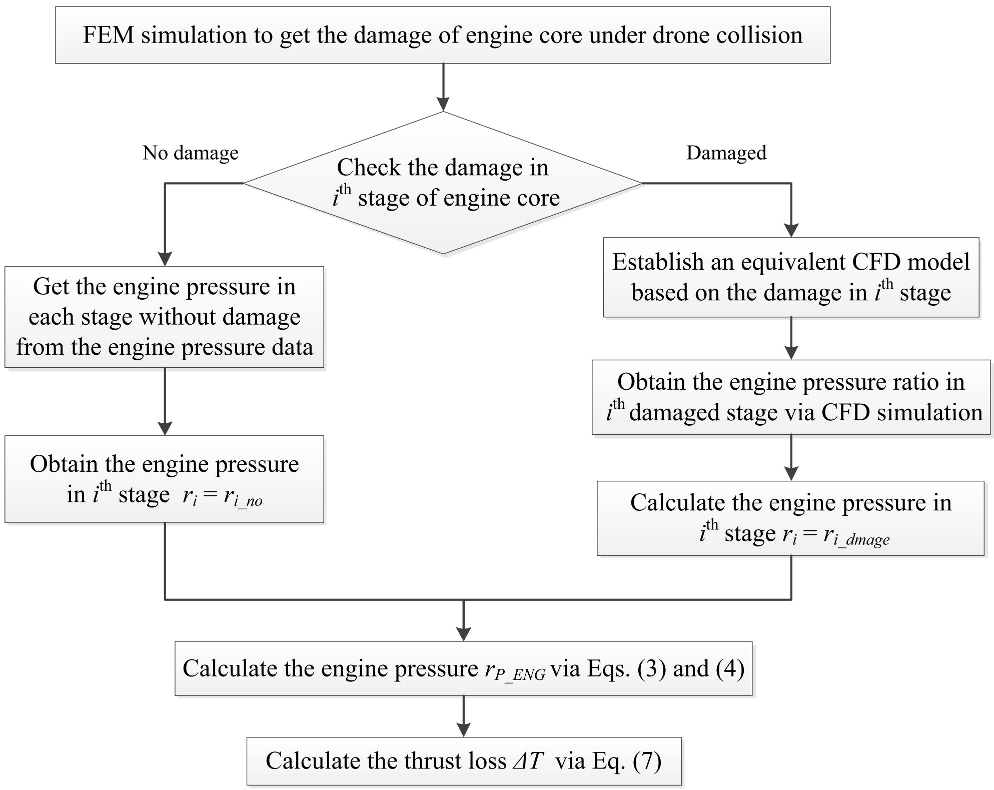

Fig. 6. Flow chart for thrust loss estimation by combining FEM with CFD.

Table 1
Parameters in different flight phases.

Parameters	Flight phase		
	Take-off	Climb	Approach
Relative velocity (knot) [46]	145	175	250
Engine rotation (RPM) [47]	5000	3000	3000
Inclination/Declination angle	5°∼10° (10°) [48]	18° [48]	−10°∼−2°(−10°) [49]

former two positions (i.e., positions 12.5% and 25%), and more bending damage of fan blades may happen for the 75% position. Hence, six separate cases including 12.5% above and below, 25% above and below, as well as 75% above and below for each flight phase, will be considered. As shown in Table 2, configurations for the above and below the nose cone for each flight phase are presented.

3. Modeling of analysis

Based on the two-stage simulation, the FEM model for the UAV impinging the engine model will be set up firstly to check the damage of fan blades and engine core. Then, the CFD simulation modeling is built to estimate the thrust loss caused by the engine core damage.

3.1. UAV-engine assembly model

The FEM simulation of the UAV airborne collision is prepared by using ABAQUS software and solved with Dynamic/Explicit formulation [50]. To assess the damage severity level caused by the collision of UAVs, a typical medium-sized drone DJI PHANTOM 3 with dimension 289.5 × 289.5 × 196 mm and weight 1.28 kg is chosen. Besides, as mentioned above, CFM-56 is the most used engine category all over the world, and a typical engine type CFM-56-5B is chosen as the commercial aircraft engine for this study.

As shown in Fig. 7, all components for the engine model are presented, which include nose cone, fan blades, fan disc, fan forward shaft, compressor wall, LPC blades, and stage-1 HPC blades. Here, all the 36 fan blades of the aircraft engine are connected to a fan disc and a nose cone, as well as a fan forward shaft. All stages of LPC and stage-1 of the HPC are taken into account. The LPC section contains 4 stages, and each stage includes one stator and one rotor. Besides, the stage-1 HPC section also has one stator and one rotor. All these components of the engine are assembled for the collision simulation. For the UAV model, more concerning is focused on the key critical components such as motors, battery, camera, main body, landing gear, electronic board, and propellers, which are measured separately to ensure accuracy, as presented in Fig. 8.

As depicted in Fig. 9, the UAV-engine system combining the aircraft engine with the UAV is assembled for the drone ingestion FEM simulation. All engine parts excepted for the fan blades are meshed by using the hexahedral element with the C3D8 type. Most parts of the fan blade are meshed with hexahedral element with the C3D8 type, and the root of the fan blade is meshed by using tetrahedron element with the C3D4 type (shown in Fig. 10(b)). The maximum and minimum element sizes for the fan blade are about 1.7 mm and 12.1 mm, respectively. A total number of 944,292 mesh elements are generated for the whole engine model. To ensure the accuracy of simulation, the mesh size of the twelve fan blades that would have contacted with UAVs during the col-

Table 2
Schematic representation of flight angle under different flight phases.

Configuration	Take-off (10°)	Climb (18°)	Approach (−10°)
Above nose cone	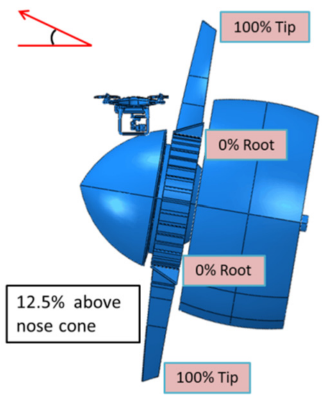	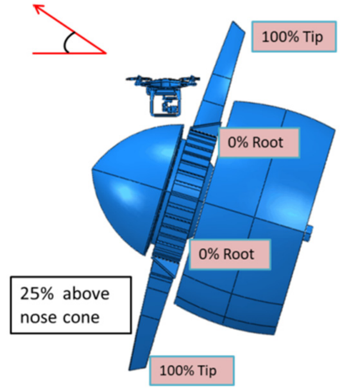	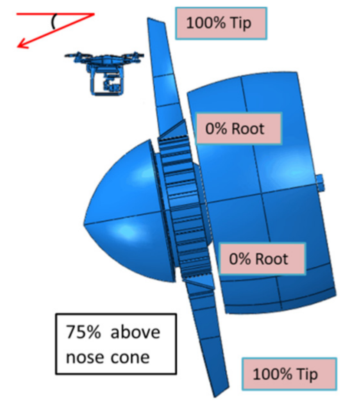
Below nose cone	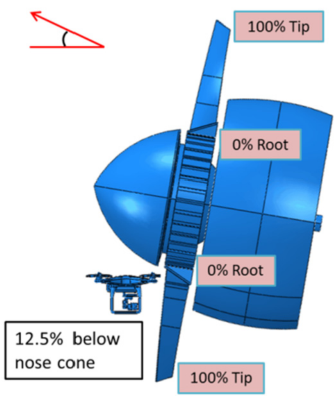	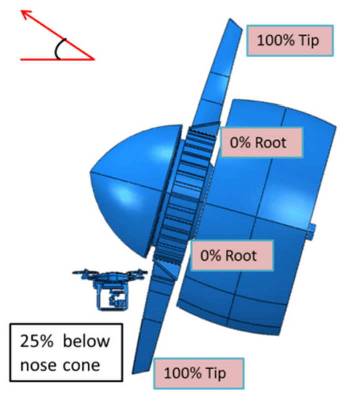	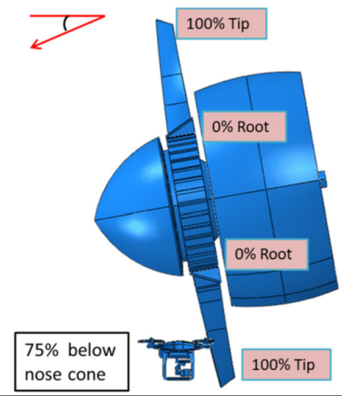

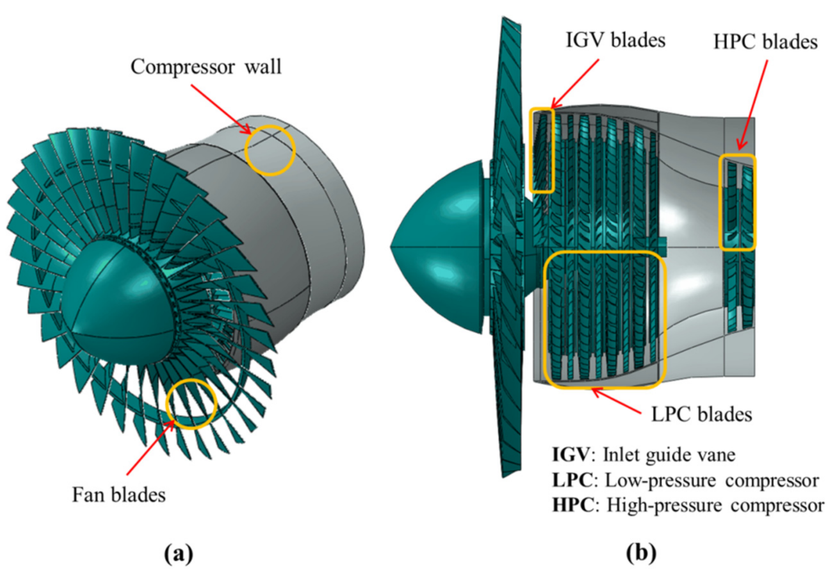

Fig. 7. Manned aircraft engine model considered in this study: (a) isometric view; (b) side view (internal components: IGV, LPC blades, and stage-1 HPC blades).

lision process is refined. The first three fan blades with a graded size wherein the contact region has the smallest size are presented in Fig. 9(b), and the element size changes smoothly from this contact region to the tip and root regions of the fan blade. Moreover, the region of the refined element for the fan blades is different for different UAV collision positions, and the graded element distributions of fan blades for the collision position 12.5%, 25%, and 75% are shown in Figs. 10(a)-(c), respectively.

All UAV parts are meshed as hexahedron with C3D8 element type except the thin-walled structures such as the main body is meshed as shell element type S4. Some minor components such as the electronic bits are treated as constraint masses attached to the main board of the UAV. The main body is meshed with a minimum element size of 0.75 mm and a maximum element size of 2.0 mm. The average element size with about 4.0∼5.0 mm is adopted to mesh the other parts of the UAV, and the total element number for

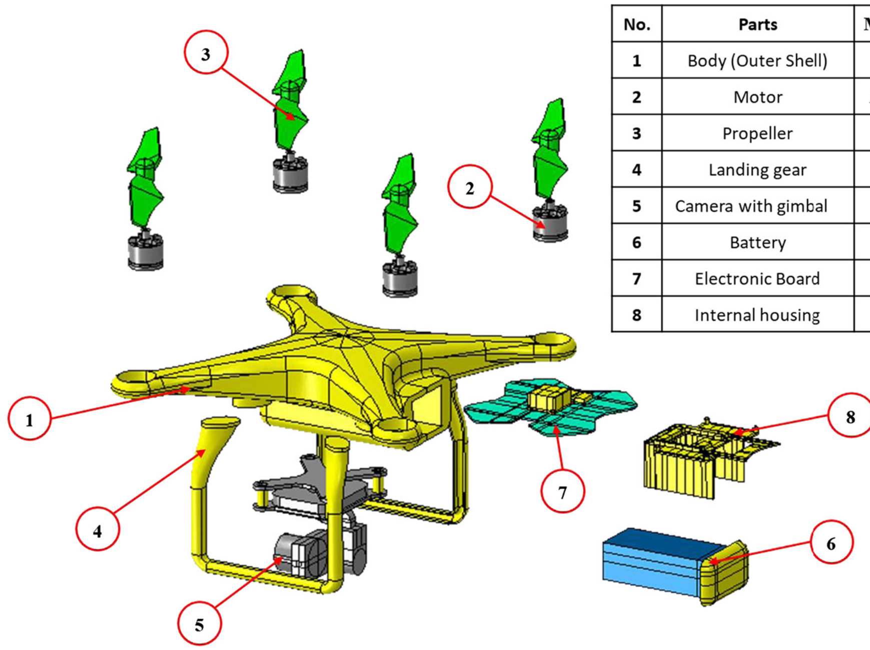

No.	Parts	Material
1	Body (Outer Shell)	PC
2	Motor	Al/Steel
3	Propeller	Nylon
4	Landing gear	PC
5	Camera with gimbal	Al
6	Battery	Li-Po
7	Electronic Board	FR-4
8	Internal housing	PC

Fig. 8. Components and their material distribution for UAV.

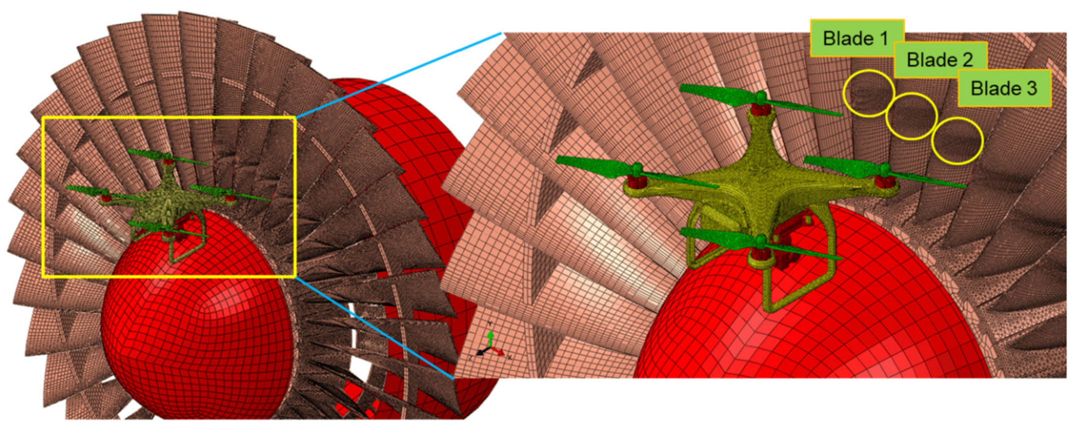

(a) (b)

Fig. 9. FEM model for UAV ingestion simulation: (a) isometric view of UAV-engine assembly model; (b) engine fan blades at UAV striking position are refined.

the UAV is about 104,928. The detailed FEM model for this UAV is depicted in Fig. 9(b).

The interaction behavior between the UAV and engine is modeled as a general contact algorithm with a friction coefficient of 0.41 [51]. The element-based surface behavior is employed in the simulation to allow eroding contact surface, i.e., once an element fails, its faces are removed from the contact domain, and the exposed faces will be activated. The fan blades, blade disc, nose cone, front forward shaft, LPC rotor, and HPC rotor blades are allowed to be moved rotationally, while no translational movement along the engine axis of rotation is employed on the whole engine parts.

3.2. CFD model for damaged engine core

After one gets the damage of LPC and HPC blades from FEM simulation, the CFD simulation will be carried out to estimate the thrust loss caused by LPC and HPC blades damage. The CFD simulation can be carried out for each stage of LPC and HPC to check the contribution of thrust loss caused by each damaged stage. Before the CFD simulation, an important step is to build an equivalent model based on the damage level of LPC and HPC blades obtained from FEM simulation. Clearly, the blade can be wholly removed once this blade is fully fractured by the ingested debris. Moreover, as pointed out by the accident report [52], the blade will lose its ability to provide the thrust when this blade is significantly distorted or bending, which can be removed in the CFD model. Similarly, a half blade can be established in the CFD model when a blade is half-destroyed or half-bending. The details for the equivalent model established in the CFD simulation are presented in Table 3.

Then, the total thrust loss can be obtained by combining all these thrust losses led by different stages together. For instance, the CFD models for the stage-1 LPC with no blade damaged and with six LPC blades missing are presented in Figs. 11(a) and (b), respectively. The total mesh number for LPC and HPC sections is around 1.5 million of tetrahedron elements. The k-ε realizable turbulence model is solved for both LPC and HPC sections. The boundary conditions for the LPC and HPC section setup in the CFD simulation under three different flight phases are presented in Table 4.

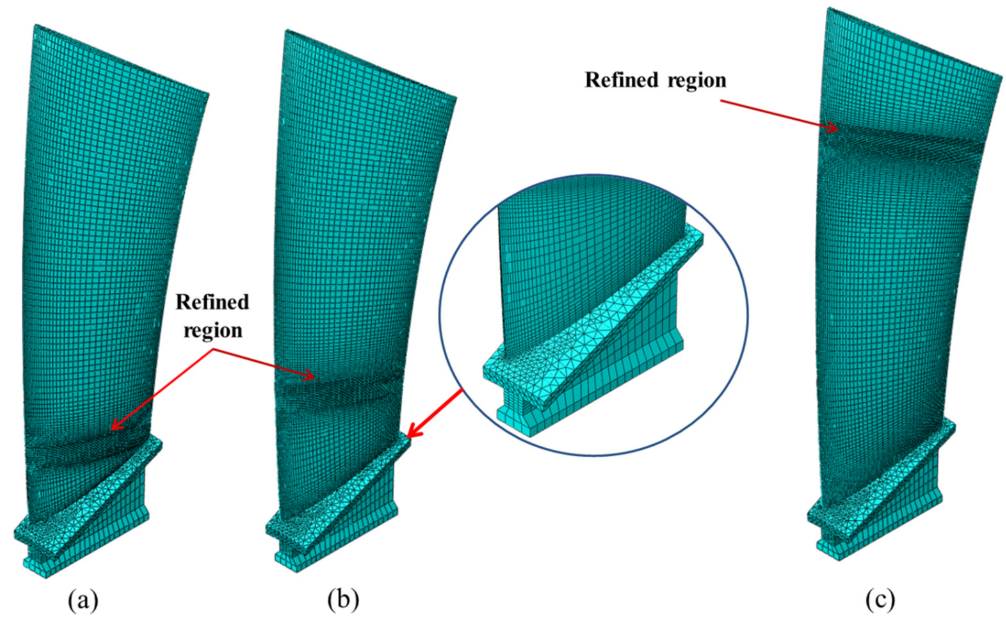

Fig. 10. Details of element refinement for the fan blade under the collision position of (a) 12.5%, (b) 25%, and (c) 75%.

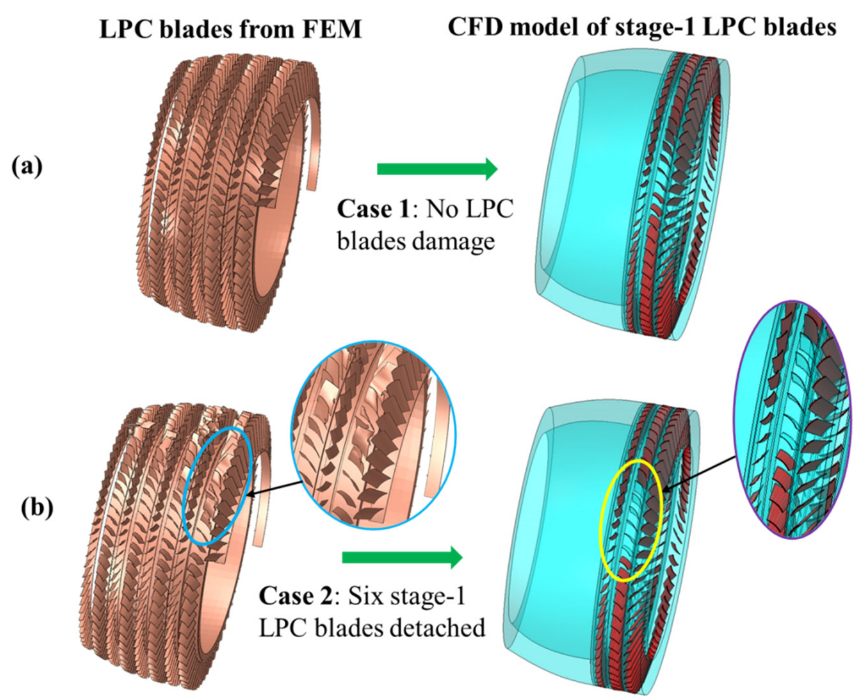

Fig. 11. CFD model of engine core: (a) engine core with no blade damaged; (b) engine core with six blades missing in stage-1 LPC.

By using this simulation, the pressure behind the compressor blades can be obtained, and the deviation of the pressure caused by the six stage-1 LPC blades missing can also be obtained, which can be used to calculate the drop of pressure ratio in the compressor core caused by six stage-1 LPC blades damaged. By adopting the CFD simulation for each damaged LPC and HPC stages, the thrust loss of engine induced by UAV airborne collision can be estimated.

3.3. Material properties of engine and UAV

The material properties for different components of the engine and UAV are different. For the engine, the fan blades and compressor blades of CFM56-5B are typically made of titanium alloy Ti-6AL-4V. In this numerical simulation, the Johnson-Cook plasticity material model is adopted to simulate the damage behavior of the titanium alloy Ti-6AL-4V. The effects of plastic strain and strain rate are both taken into account in this model, which can be expressed as [28]:

$$\sigma = \left[A + B(\varepsilon_p)^n\right]\left[1 + C\ln(\dot{\varepsilon}^*)\right]\left[1 - \left(T^*\right)^m\right] \tag{8}$$

where σ is the effective stress, and ε_p stands for the effective plastic strain; $\dot{\varepsilon}^* = \dot{\varepsilon}_p/\dot{\varepsilon}_0$ denotes the dimensionless plastic strain rate, in which $\dot{\varepsilon}_p$ and $\dot{\varepsilon}_0$ are, respectively, the plastic strain rate and the reference strain rate (usually defined as 1 s^{-1}). T^* denotes the homologous temperature of the material, which is not taken

Table 3
Strategy for establishing equivalent model in the CFD simulation.

Fracture from FEM	Description	Strategy	Equivalent model in CFD
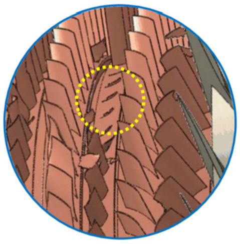	Whole blade broken	Wholly removed	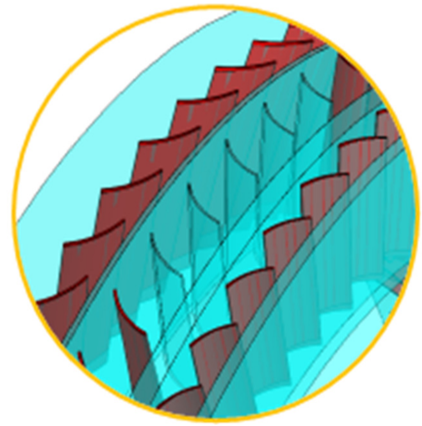
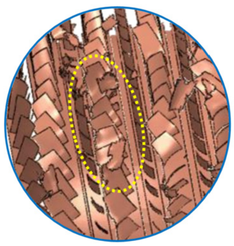	Whole blade distorted	Wholly removed	
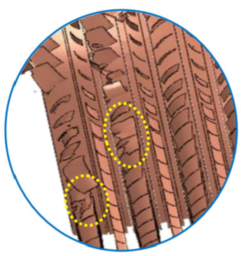	Half of blade broken	Half removed	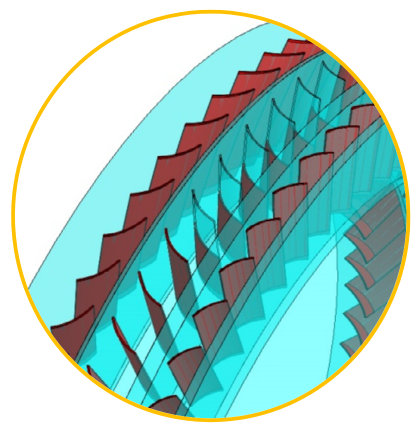
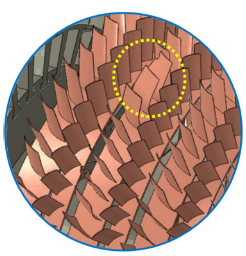	Half of blade distorted	Half removed	

Table 4
Boundary condition adopted in the CFD simulation for different flight phases.

Flight phase	Section	Mass flow rate (kg/s)	Total pressure (Pa)
Take-off	LPC	32.72	101,325
	HPC	32.72	220,000
Climb	LPC	39.47	101,325
	HPC	39.47	220,000
Approach	LPC	56.41	101,325
	HPC	56.41	220,000

Table 5
Johnson-Cook material parameters used in Eq. (8) for Ti-6AL-4V.

Material	A (MPa)	B (MPa)	n	C	E (GPa)	ν	ρ (kg/m^3)
Ti-6AL-4V [34]	1098	1092	0.93	0.014	113	0.33	4430

into consideration in the present model. A, B, n, and C are the quasi-static yield stress, the initial hardening modulus, the work hardening coefficient, and the strain rate dependency coefficient, respectively, which are listed in Table 5. In the UAV collision process, most of the materials are failure because of tensile stretching, and the mesh will be eliminated as the tensile threshold strain is achieved. The failure strain of Ti-6AL-4V is set as 0.11 [53]. The nosecone and containment ring are made from aluminum which is modeled as elastic-plastic material with its material properties listed in Table 6, and the mesh elimination criterion of this material is defined by the maximum failure strain.

The material properties of UAVs are derived from Ref. [8], in which detailed materials used for each part are shown in the table of Fig. 8. The rotor and stator parts of the motor are made of Aluminum and Steel alloy, respectively, which are modeled as the elastic-plastic material model, and detailed material parameters are listed in Table 6. Other polymer materials of the UAV like polycarbonate polymer (PC), Nylon, and FR-4 are also modeled as the elastic-plastic criterion with ideal plasticity and strain-rate independent, which can be adopted for both quasi-static and dynamic conditions. The maximum tensile plastic strain is employed for the criterion of element elimination for these materials, as presented in Table 6. The element will be eliminated as the plastic strain is larger than the maximum failure strain. The battery of the UAV is made from lithium-ion polymer (Li-Po) with 60% porosity inside the cell body. Hence, the crushable foam element is adopted to model the mechanical behavior of battery, and some basic mechanical parameters are given as follows [54]: density $\rho = 1755$ kg/m^3, Young's modulus $E = 500$ MPa, and Poisson's ratio $\nu = 0.01$, and failure strain $\varepsilon_{max} = 0.375$.

Table 6
Material properties of aluminum, steel, PC, nylon, and FR-4 used in UAV model.

Material	Density (kg/m^3)	Young's modulus (GPa)	Poisson's ratio	Yield stress (MPa)	Ultimate tensile stress (MPa)	Failure strain (%)
Aluminum [55]	2600	66	0.33	170	330	0.14
Steel [56]	7800	210	0.3	460	560	0.215
PC [12]	1197.8	2.59	0.37	50	50	0.50
Nylon [12]	1340	2.20	0.42	105	130	0.25
FR-4 [57]	1900	22	0.21	105	282	0.0195

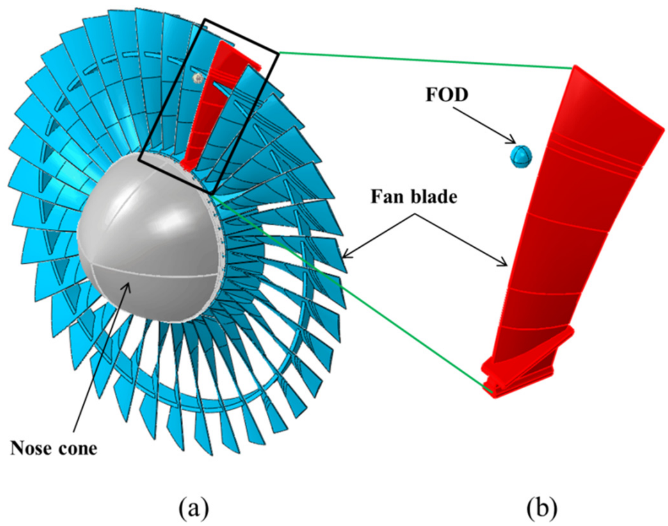

Fig. 12. FEM model of FOD striking on engine fan blades: (a) isometric view of FOD-engine assembly, (b) enlarged view.

4. Model validation

In this section, the validation study will be carried out by comparing the numerical results with previous experimental works. Firstly, the engine model is validated by using Foreign Object Debris (FOD) impinging onto engine fan blades to check the damage of fan blades predicted by the present model and experiment. Secondly, the UAV model under low-speed impact is validated by comparing the numerical results with the drop-test experiment done by Olivares et al. [8]. Thirdly, the validation for the present UAV striking onto the rotating aircraft propellers is carried out to check the damage of UAV model under the high-speed impact.

4.1. Validation of engine model

To validate the FEM model of CFM-56-5B engine, the fan blades installed in this engine are taken as the specimen for this validation study. The geometry and finite element model of this engine are presented in Section 3.1, and its material properties are given in Section 3.3. After setting the material properties for fan blades of this engine, the damage of engine fan blades under the striking of FOD will be analyzed. To investigate the performance of fan blades under high-speed collision, several collision velocities are taken into account. The particle of FOD is modeled as 3 mm steel ball projectile traveling with different impact speeds, as depicted in Fig. 12.

The damage sizes including the width and depth of the fan blade predicted by experiment and FEM simulation under different collision velocities are compared in Fig. 13. It is clear that the width and depth of damage both enlarge as the collision velocity of FOD increases. Besides, the damage sizes of the fan blade under FOD collision predicted by FEM simulation agree well with that predicted by experiment [58]. Moreover, Table 7 compares the damage pattern of the fan blade under FOD collision under three different collision velocities (280 m/s, 200 m/s, and 120 m/s) for experiment and FEM simulation. One can also find that the damage severity enhances as the impacting speed of the FOD increases. By comparing the results of the experiment and simulation, a good correlation of the fan blades damage can be observed between these two results, indicating that the material properties definition and the FEM model of the engine established in the present study is reasonable, which can be further used for the UAV collision simulation.

4.2. Validation of UAV model under low-speed impact

The deformation of the UAV model under low-speed impact is validated by comparing the numerical results with the experiment done by Olivares et al. [8]. In their experiment, a free-drop test is conducted by using UAV (PHANTOM 3) dropping on a steel plate with a released height of 5.18 m. A similar condition is followed in the present FEM simulation where the UAV is striking onto a rigid wall with an initial velocity of 10.12 m/s, and the details on the FEM model of UAV are mentioned in Section 3.1. The deformed shapes of the UAV at different instances of the impact predicted by the FEM simulation and by the experimental analysis are compared in Table 8. It is found that the deformed shape predicted by the FEM simulation consists well with that obtained by experiment [8], indicating the present FEM model can accurately predict the deformation history of UAV subjected to the impact loading. Besides, in Olivares et al.'s experiment [8], the reaction force can be measured by employing the force sensor at the bottom of the rigid plate. This reaction force also can be exported in our FEM simulation, which gives a comparison with Olivares et al.'s experiment [8], as depicted in Fig. 14. One can found that there is some deviation between experiment and simulation during the period of 20-30 ms, which may cause by the fact that the drop angle θ of the UAV (i.e., the angle with respect to the vertical direction shown in Fig. 14) adopted in the simulation is not exactly the same to that during the experiment. Hence, three drop angles, i.e., $\theta = 20°$, $\theta = 22.5°$ and $\theta = 25°$ with a deviation of 2.5°, are chosen in our simulation study. As can be seen in Fig. 14, even though some deviations can be observed for the time history of reaction force, all simulation results show almost the similar change trend to the experiment, which illustrates that the present model can be used to analyze the impact behavior of UAVs.

4.3. Validation of UAV under high-speed impact

To evaluate the damage of UAV model under the scenario of high-speed impact, the third validation is conducted by using the present UAV (PHANTOM 3) striking onto the rotating aircraft propellers, which is given a comparison with previous experiment study [59]. In this experiment, a UAV is impacted on the propellers of Aircraft Antonov AN-2. This system is composed of 4 blade propellers with a span of 1.5 m and made from Aluminum. The relative speed between the drone and propeller is set as 16 m/s, and the rotation speed is treated as the 50% of thrust level [60],

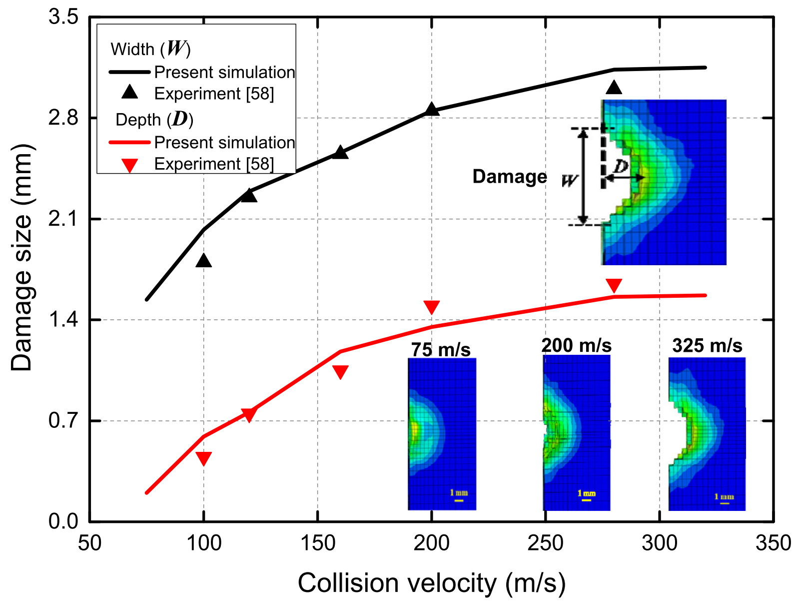

Fig. 13. Comparison between simulation and experiment for the damage size of fan blades under different collision velocities.

Table 7
Comparison between experiment and simulation for damage of fan blades under different collision velocities.

Collision velocity	280 m/s	200 m/s	120 m/s
Experiment [58]			
Simulation	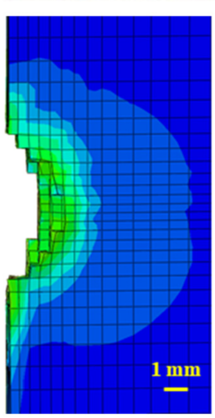	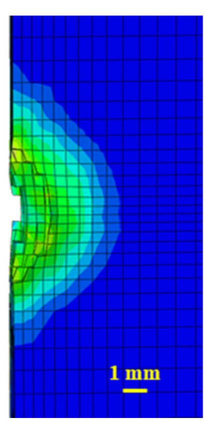	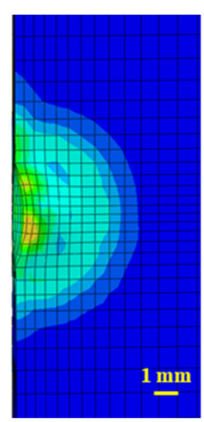
Damage type	Piece out	Torn	Dented

i.e., 1670 RPM. The collision process of the UAV predicted by FEM simulation and experiment are compared in Table 9 for different instances. It can be found that the UAV is cut into much small debris due to the rotating aircraft propellers. The damage of UAV predicted by FEM simulation fits with the experimental observation, indicating the present FEM simulation can capture the collision process accurately and can be used to predict the damage behavior of UAV collision into operating engine with high rotation speed.

5. Results and discussion

In this section, the influence of the UAV collision configuration and collision position, as well as the flight phase on the dynamic response and thrust loss of the CFM-56-5B engine will be studied. As discussed in Section 2.3, we will analyze the influence of two collision configurations (i.e., above and below the nose cone cases), three collision positions (i.e., 12.5%, 25%, and 75% collision positions), and three flight phases (i.e., take-off, climb, and approach). The plan of our study is shown in Table 10. In Section 5.1, the ef-

Table 8
Comparison of the deformed shape predicted by the FEM simulation ($\theta = 25°$) and experimental study in different instances.

Time	Experiment [8]	Present FEM simulation
0 ms		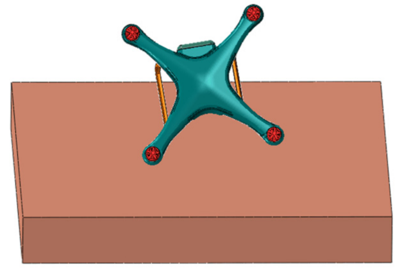
15 ms	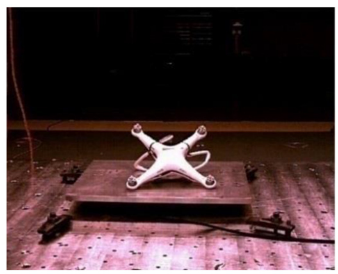	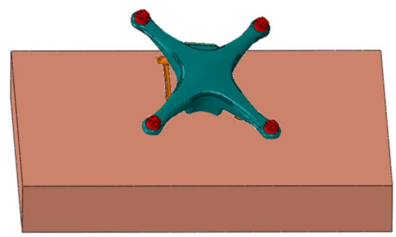
25 ms	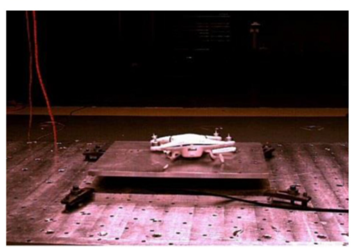	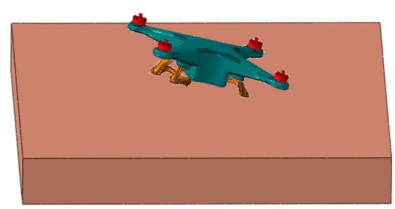
40 ms	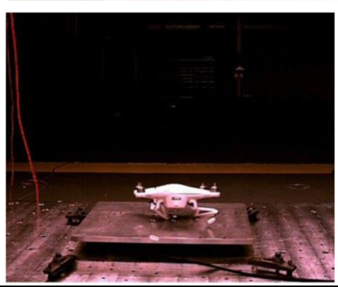	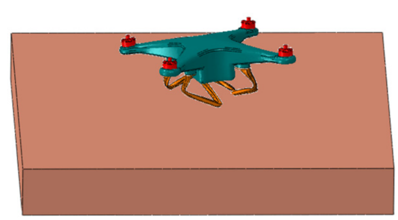

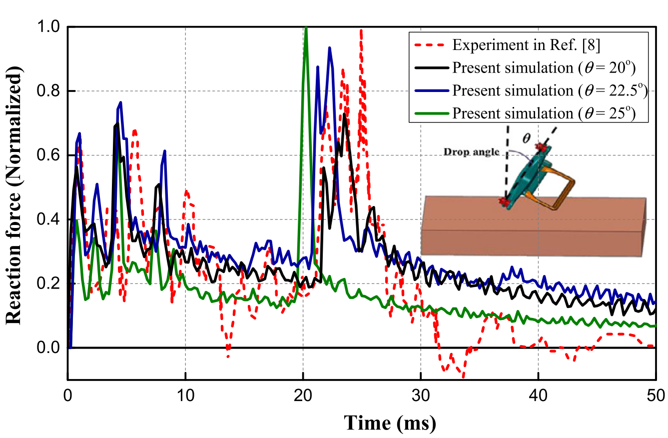

Fig. 14. Comparison of the time history of the reaction force predicted by the FEM simulation and experimental study [8].

fect of collision configuration on the damage of fan blades under the take-off flight phase will be studied to determine the worst collision configuration. Next, the damage of fan blades and engine core will be analyzed for different collision positions and different flight phases in Sections 5.2. Finally, in Section 5.3, the resulted thrust loss of the engine will be studied for different collision positions and flight phases based on the worst collision configuration and position.

5.1. Determination of worst collision configuration

In this subsection, the effect of collision configuration (i.e., above and below the nose cone) on the damage of fan blades will be investigated to determine the worst collision configurations. As presented in Table 11, six collision positions including three positions above the nose cone as well as three positions below the nose cone are compared for the take-off flight phase. The simulation parameters are derived from Section 2.1, and the material parameters are derived from Section 3.3. It is found that the fracture of fan blades happens for all collision positions except for the above nose cone at the 12.5% collision position. By comparing with the position cases above the nose cone, the damage caused by the below nose cone collision position cases is much more serious. Hence, the cases for the collision position below the nose cone will be focused on in the following studies for the take-off

Table 9
Comparison between experiment and simulation for damage of UAV (PHANTOM 3) striking onto rotating aircraft propellers.

Time	Experiment [59]	FEM simulation
0.0 ms	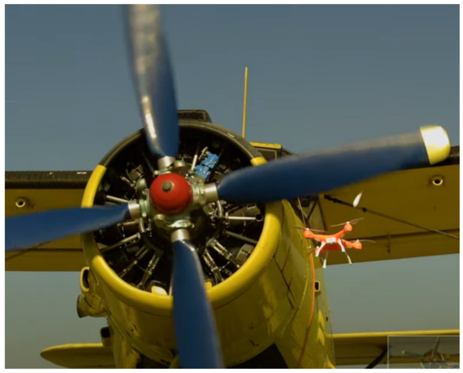	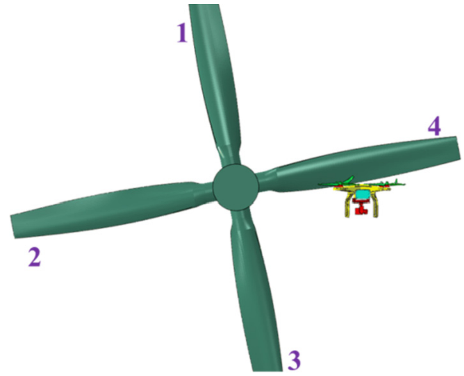
7.9 ms	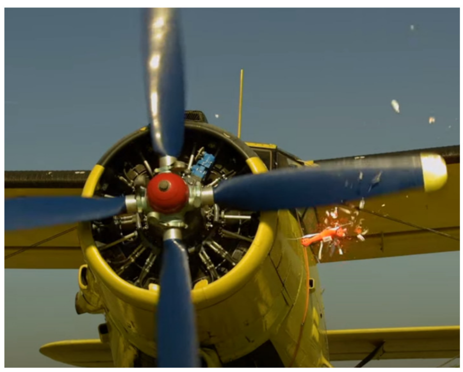	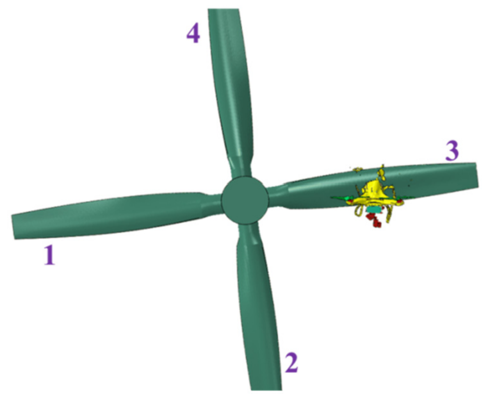
15.6 ms		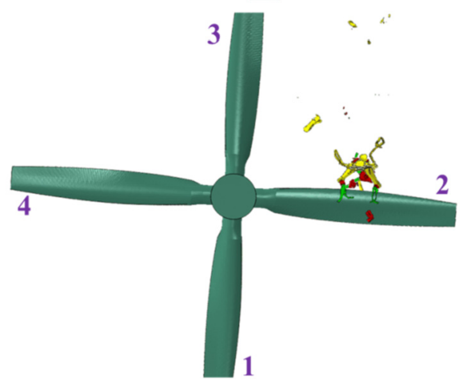
20.3 ms	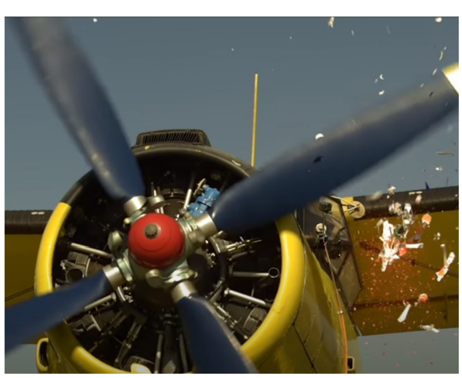	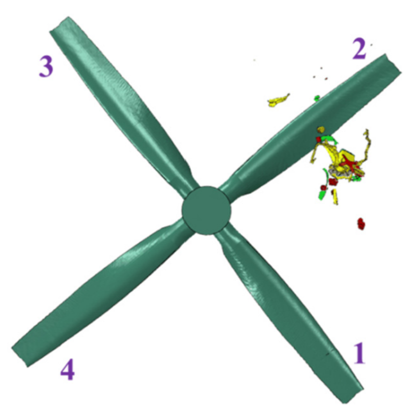

flight phase. Accordingly, the collision position below the engine nose cone is taken into account for the climb flight phase because the angle direction in this phase is similar to that in the take-off flight phase. In contrast, the position above the engine nose cone is considered for the approach flight phase due to the opposite angle direction by comparing it with the take-off flight phase.

The deformation process of the engine fan blades under the collision position 25% during the take-off flight phase is presented in Fig. 15 under different time steps. It can be seen that the UAV has

Table 10
Results presented in this section.

Cases	Take-off			Approach			Climb
	12.5%	25%	75%	12.5%	25%	75%	12.5%
Above	Section 5.1	Section 5.1	Section 5.1	Sections 5.2 & 5.3	Sections 5.2.1 & 5.3.1	Sections 5.2.1 & 5.3.1	–
Below	Sections 5.1, 5.2.2 & 5.3.2	Section 5.1	Section 5.1	–	–	–	Sections 5.2.2 & 5.3.2

Table 11
Damage of rotating fan blades under different collision configurations during take-off flight phase.

Cases	Position 12.5%	Position 25%	Position 75%
Above nose cone 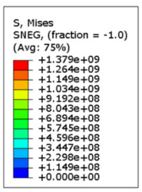	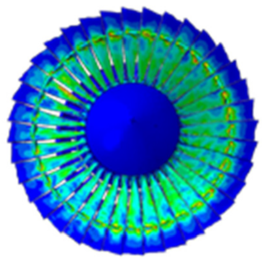	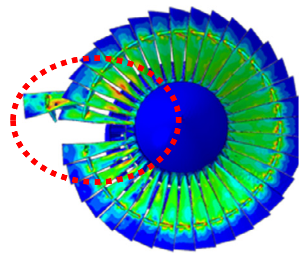	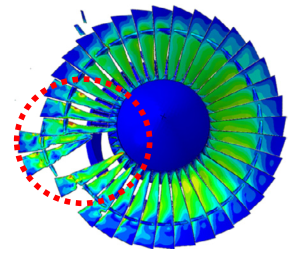
Description of failure	Two fan blades are small bending	One fan blade is broken from the root	Two fan blades are broken from the root, and one is broken in the tip
Below nose cone 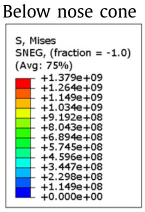	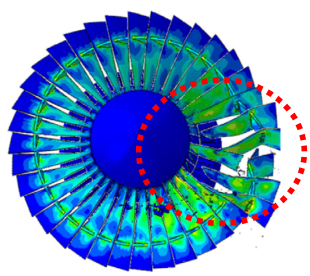	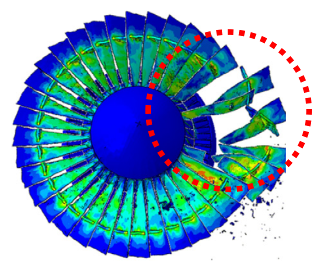	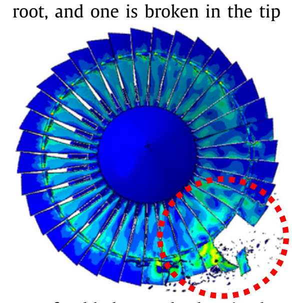
Description of failure	Five fan blades are broken from the root.	Six fan blades are broken from the root.	Two fan blades are broken in the tip, and two blades are material loss.

been cut into much small debris by the rotating fan blades, and some debris may be ingested into the compressor core once the collision position is closer to the nose cone. Besides, one can also find that several fan blades are broken under the take-off flight phase, which may lead to the windmill phenomenon of the engine and result in the loss of the whole engine thrust [61]. From the simulation, one can get the deformation and damage of every fan blades, and then the contact force of the fan blade that has the largest deformation or damage is presented. As plotted in Fig. 16, the contact forces in the fan blade with the largest damage are compared for different collision positions. The take-off flight phase is taken into account, and the calculation parameters including the relative velocity are derived from Table 1. One can observe that the peak contact force is the largest for the position 75%, followed by the positions 25% and 12.5%, respectively, indicating the contact force gets larger as the collision position is close to the tip of the fan blade.

5.2. Damage assessment study

5.2.1. Effect of UAV collision position

Another comparison of different collision positions is given in Table 12 for the flight phase of approach. Here, only the worst cases are taken into account, i.e., the position above the nose cone is examined. From this table, only the small bending deformation of fan blades can be found for all three collision position cases under the approach flight phase, which is much smaller by comparing with the take-off flight phase. This is due to the fact that the rotation speed in the approach flight phase is much lower than that in the take-off flight phase. Additionally, the debris will be ingested into the engine core and would cause the damage of both the LPC and HPC blades for the 12.5% collision position case, while only some damage of LPC blades can be observed for the 25% collision position case. Besides, no damage on the LPC and HPC blades is found for the 75% collision position case because no debris is ingested into the compressor core under this collision position.

The UAV collision process of the aircraft engine under the approach flight phase for the collision positions 25% and 12.5% are presented in Figs. 17 and 18, respectively. It is demonstrated that the UAV will be cut into an amount of debris, and some of them will be ingested into the engine core, while the damage on fan blades is very small for these two collision positions. By comparing these two figures, the ingested debris will cause the damage of LPC and HPC blades for the collision position 12.5%, while only some damage of LPC blades can be observed for the collision position 25%. The thrust loss caused by the damage of the compressor core for position 12.5% and position 25% can be determined by CFD simulation.

5.2.2. Effect of flight phases

The influence of the flight phase on the damage severity of the engine is examined in this subsection. Here, the 12.5% collision position is taken into account. For take-off and approach flight phases, the collision position above the nose cone is considered, while the collision position below the nose cone is taken into account for the climb. Besides, the calculation parameters including the relative velocity for different flight phases are derived from Table 1. As presented in Table 13, the damages of fan blades and compressor core are compared for different flight phases. It

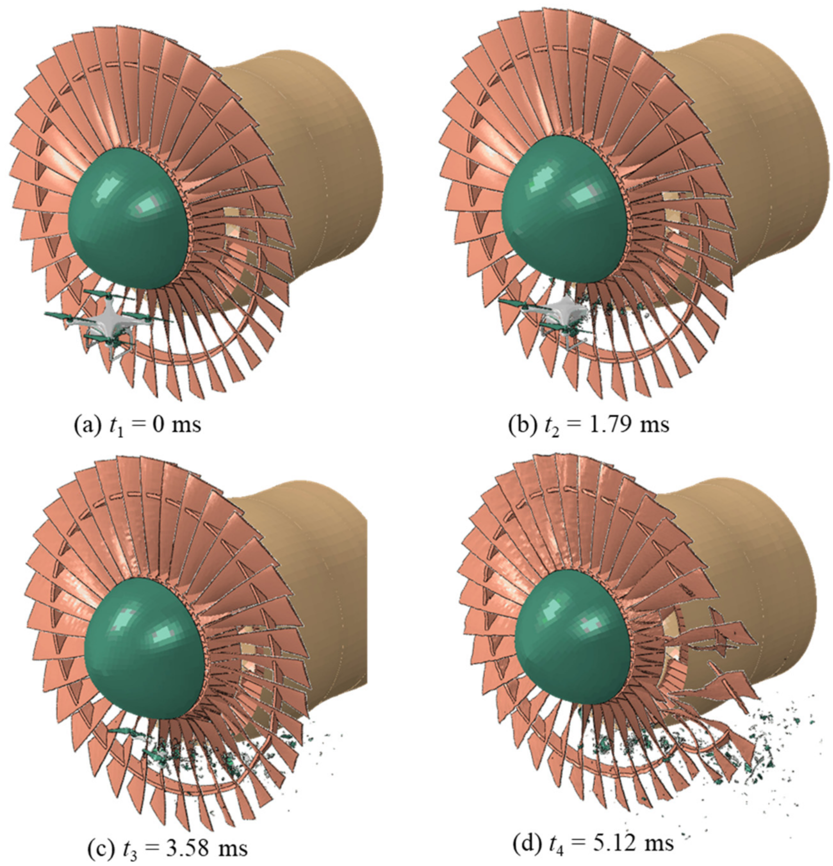

Fig. 15. Deformation process of the UAV strike on the 25% collision position under take-off flight phase: (a) $t_1 = 0$ ms; (b) $t_2 = 1.79$ ms; (a) $t_3 = 3.58$ ms; (b) $t_4 = 5.12$ ms.

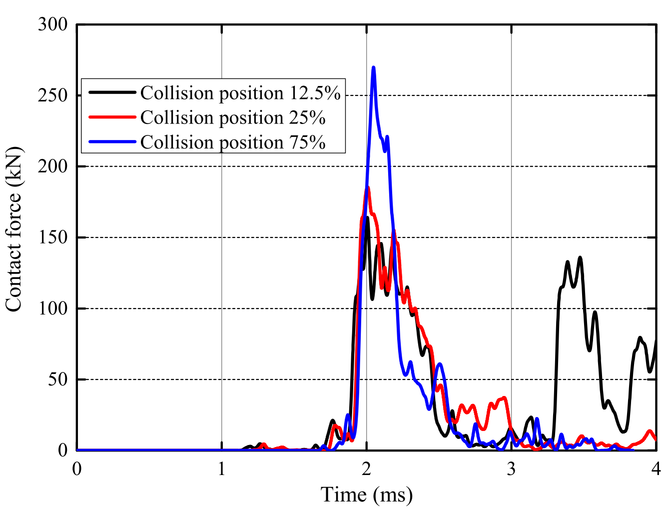

Fig. 16. Contact force in rotating fan blade for UAV collision under take-off flight phase.

can be concluded that the flight phase plays an important role in the damage of the engine, and much more significant damage can be detected during the take-off phase, followed by the flight phases of approach and climb. During the take-off flight phase, the windmill phenomenon would happen because at least three fan blades are damaged. During the approach phase, even though no significant damage on the fan blades is found, the debris will be ingested into the engine core and cause the damage of LPC and HPC blades. A similar phenomenon can also be observed for the climb phase, but the ingested debris can only result in the damage of LPC blades.

In addition, the contact force of the fan blade caused by different flight phases is also compared in Fig. 19. The numerical results indicate that the flight phase will affect the contact force significantly, i.e., the peak contact force is largest under the take-off flight phase, followed by climb and approach flight phases, respectively. Besides, the peak contact force appears at different times for different flight phases, which is mainly attributed to the fact that the initial velocities for these three flight phases are different. The initial velocity is the largest for the approach flight phase, which will result in the peak appearing earliest, followed by the climb and take-off flight phases, respectively. Furthermore, one can observe three peaks for the climb flight phase, and two peaks of the contact force can be found for the take-off and approach flight phases. This multi-peak phenomenon is caused by the fact that the UAV is a typical non-homogeneous made of multi-components with different stiffness, and the fan blade may be impacted by different components at different times during the whole engine ingestion process.

5.3. Thrust loss study

5.3.1. Effect of collision position

According to Eq. (6) and the data in Ref. [45], the curve of engine thrust versus the engine pressure ratio can be plotted in Fig. 20(a). Based on this curve, the relationship between the thrust loss (ΔT) and the drop of engine pressure ratio can be obtained via Eq. (7), as depicted in Fig. 20(b). From this figure, the thrust loss of aircraft engine can be obtained once the drop of the engine pressure ratio is determined.

Once the damage of LPC and HPC blades is determined, the CFD model (shown in Fig. 11) can be established to examine the pressure ratio in each damaged stage. The total pressure distribution

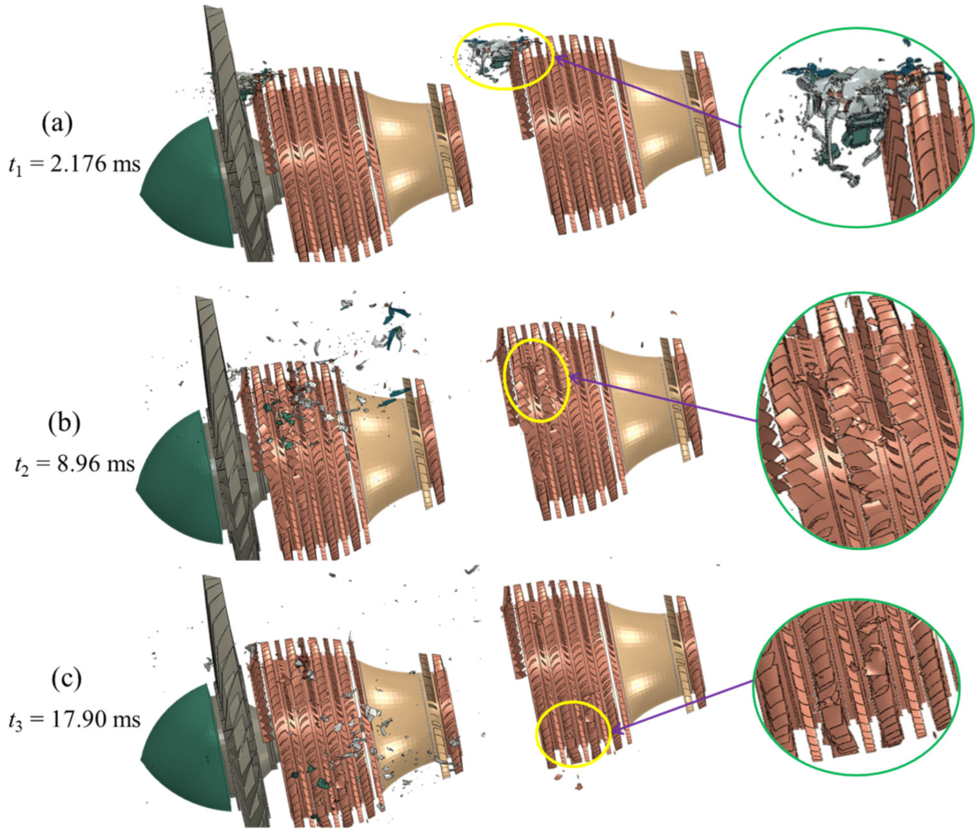

Fig. 17. Deformation process of the UAV strike on the 25% collision position under approach flight phase: (a) $t_1 = 2.176$ ms; (b) $t_2 = 8.96$ ms; (c) $t_3 = 17.90$ ms.

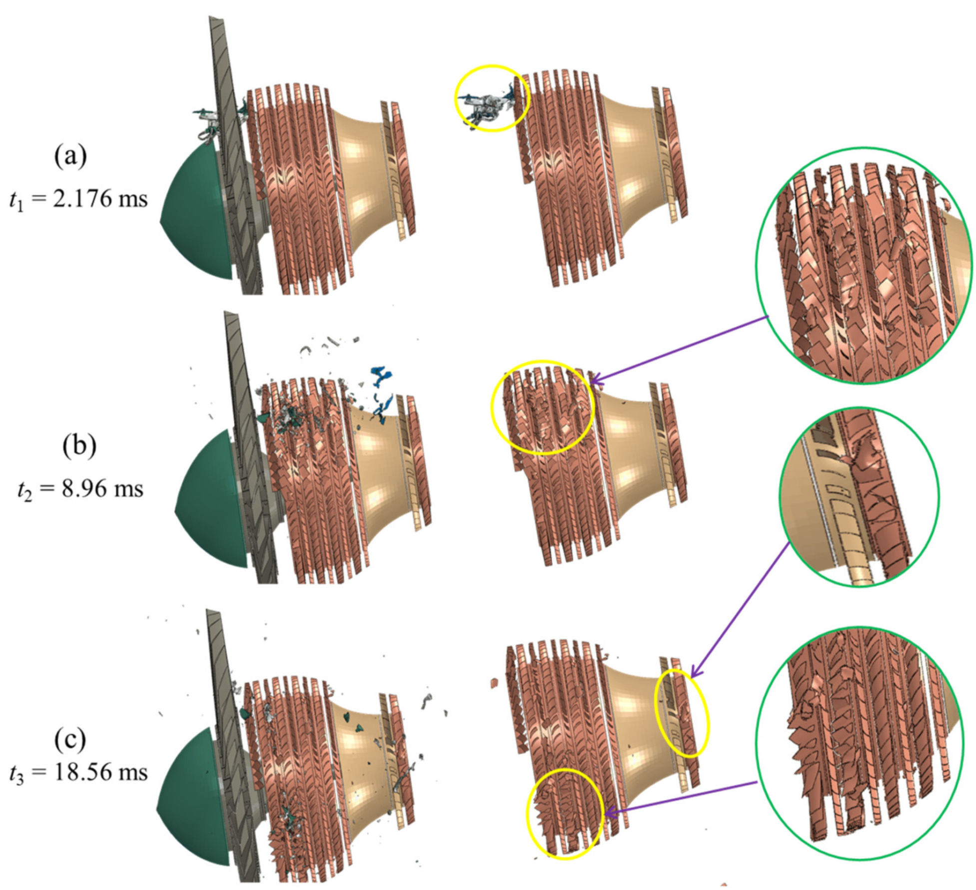

Fig. 18. Deformation process of the UAV strike on the 12.5% collision position under approach flight phase: (a) $t_1 = 2.176$ ms; (b) $t_2 = 8.96$ ms; (c) $t_3 = 18.56$ ms.

Table 12
Comparison of engine damage under different collision positions during approaching.

	Position 12.5% (above)	Position 25% (above)	Position 75% (above)
Fan blade 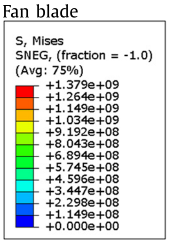	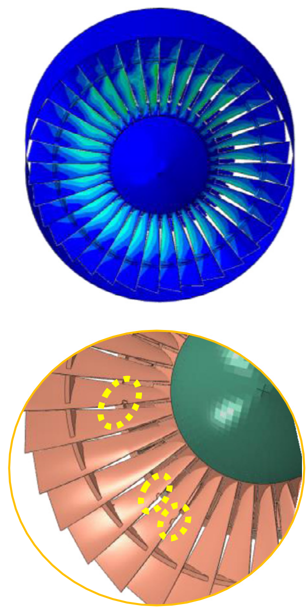	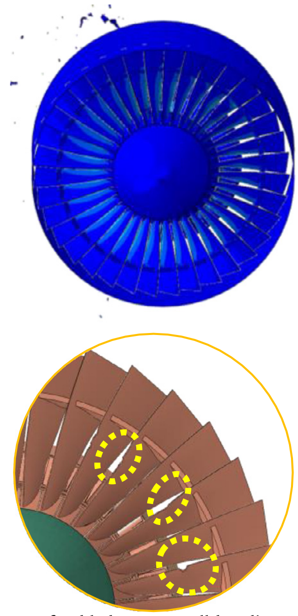	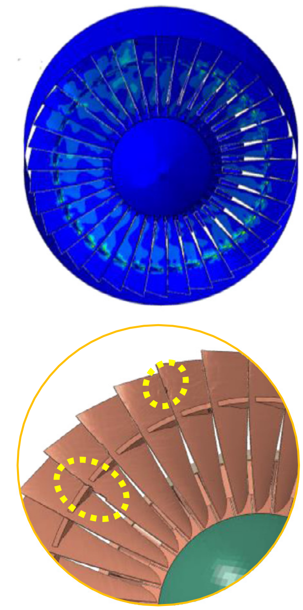
Description of failure	Three fan blades are material loss.	Two fan blades are small bending and one is material loss.	Two fan blades are material loss.
LPC & HPC Blades 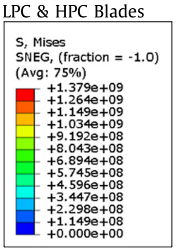	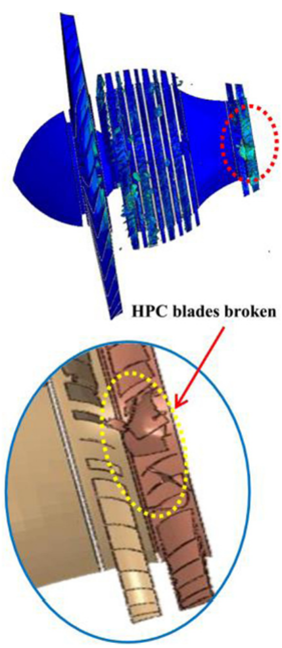	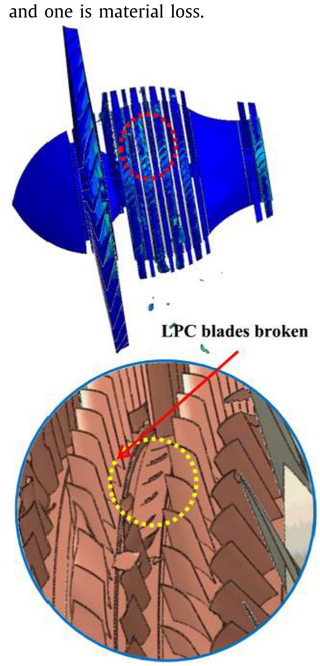	No debris ingested into the compressor core.

in no damaged stage-1 LPC, damaged stage-1 LPC, and damaged stage-1 HPC are comparatively presented in Figs. 21(a), (b) and (c), respectively. Here, the total pressures at some typical positions of compressor core highlighted in Fig. 4 are captured, which can be adopted to evaluate the pressure ratio in each stage. After getting the pressure ratio in each stage, the total pressure along the engine core can be plotted in Fig. 22 for these three collision positions. From this figure, it is clear that the total pressure changes significantly during the HPC part; hence, the damage of HPC will result in much more thrust loss. After one gets the total engine pressure ratio for each UAV collision case, the total engine pressure ratio for position 12.5%, position 25%, and position 75% cases are finally calculated as 1.23, 1.35, and 1.48, respectively. Accordingly, the drop of engine pressure ratio for these three cases can be calculated as 16.89%, 8.78%, and 0%, respectively. By using Fig. 20(b), the thrust loss for collision position 12.5%, 25%, and 75% cases can be finally assessed as 60%, 25%, and 0%, respectively.

5.3.2. *Effect of flight phases*

The CFD simulation is also carried out to evaluate the thrust loss caused by the damage of the compressor core. After obtaining the pressure ratio in each damaged stage, the pressure along the engine can be plotted in Fig. 23. The total engine pressure ratios under the flight phase of take-off, approach, and climb are 1, 1.23, and 1.38, respectively. Accordingly, the thrust loss for take-off, approach, and climb can be calculated as 100%, 60%, and 22%, respectively.

Table 13
Damage of fan blades and compressor core blades under different flight phases (collision position: 12.5%).

	Take-off	Approach	Climb
Fan blade 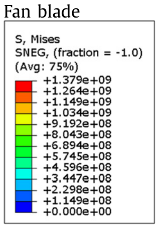	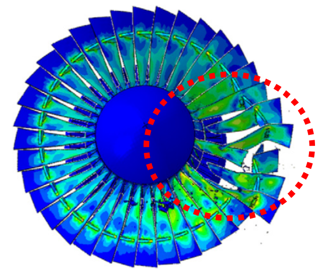	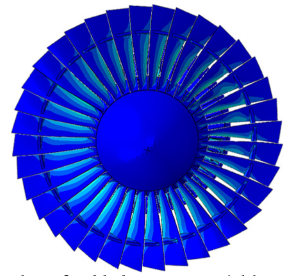	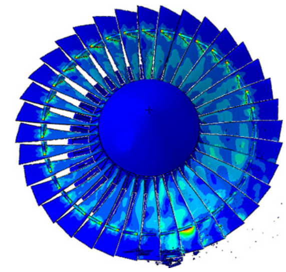
Description of failure	Five fan blades are broken from the root.	Three fan blades are material loss.	Two fan blades are small bending.
LPC & HPC Blades 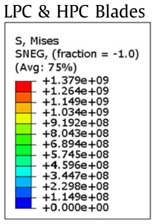	Damage here will lead to excessive engine vibration (Windmill).	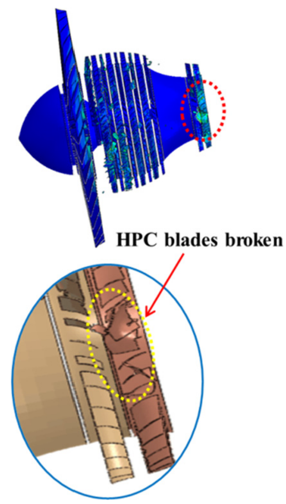	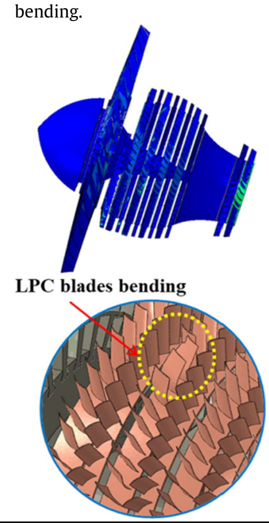

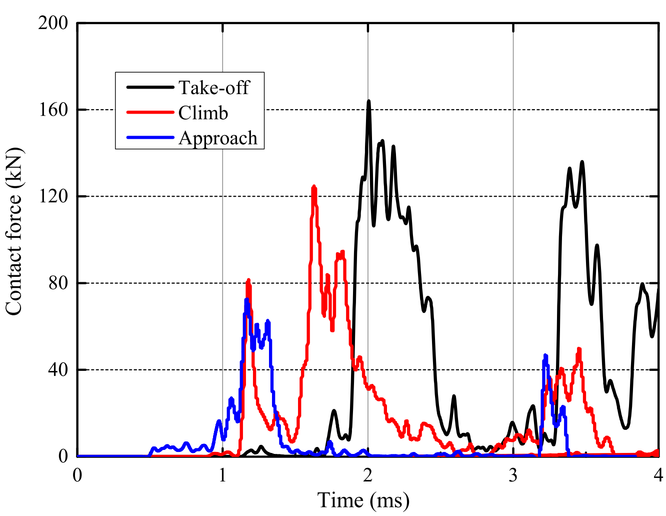

Fig. 19. Comparison of contact force in rotating fan blade for UAV airborne collision under different flight phases.

6. Conclusion and future work

In this paper, the UAV airborne collision on manned aircraft engine is studied based on the combination of FEM and CFD simulations to evaluate the influence of UAV collision on the operational safety of manned aircraft. Firstly, it is found that the engine is the most critical component, and take-off, climb, and approach are the most hazardous flight phases through visiting the bird strike data. Then, a UAV-engine assembly system is set up, and the drone model with considering all internal components is validated by comparing it with the previous experiment. The damage of fan blades and compressor blades is simulated with the aid of FEM simulation, and the percentage of thrust loss of the engine is evaluated by the reduction of pressure ratio determined by CFD simulation. Through numerical studies of UAV airborne collision under different collision positions and flight phases, some meaningful conclusions are drawn as follows:

a) Different collision positions would lead to different damages of fan blades and compressor core, as well as different thrust losses. The 75% collision position is much more critical to the damage of fan blades, while more debris will be ingested to the compressor core for the 12.5% collision position, which would cause more damage to the compressor core and lead to more thrust loss.
b) The flight phase will affect the damage level of UAV airborne collision significantly. Much more significant damage can be detected during the take-off phase, followed by the flight phases of approach and climb. The windmill phenomenon would happen for the take-off flight phase, while the damage of LPC and HPC blades can be found for the climb and approach flight phases, respectively.
c) The collision position will significantly affect the thrust loss of engine core, and the resultant thrust loss for the collision position 12.5%, 25% and 75% cases can reach 60%, 25%, and 0%, respectively, for the airborne UAV collision happens during the approach flight phase. Furthermore, the flight phase also plays an important role on the resulted thrust loss under UAV airborne collision, in which the largest thrust losses for take-off, approach, and climb are assessed as 100%, 60%, and 22%, respectively.

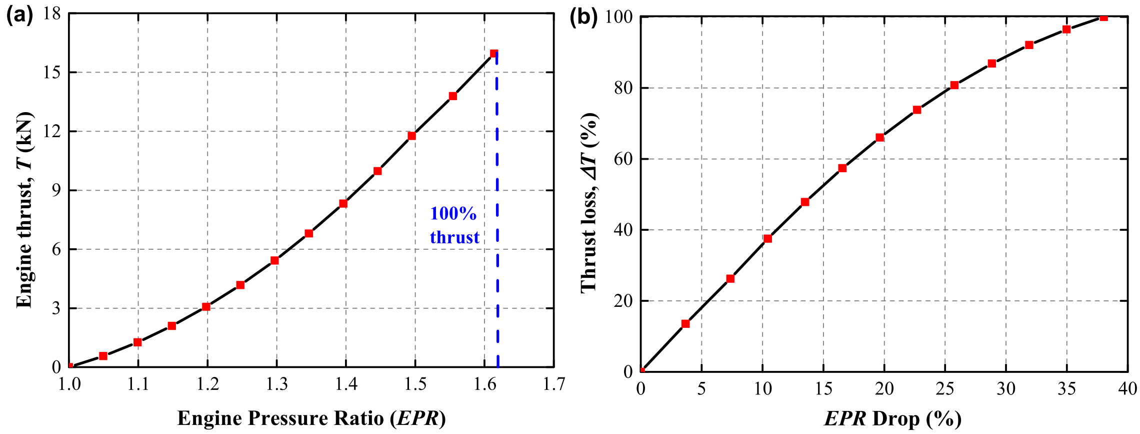

Fig. 20. The curve of (a) engine thrust versus engine pressure ratio, (b) thrust loss versus the drop of engine pressure ratio.

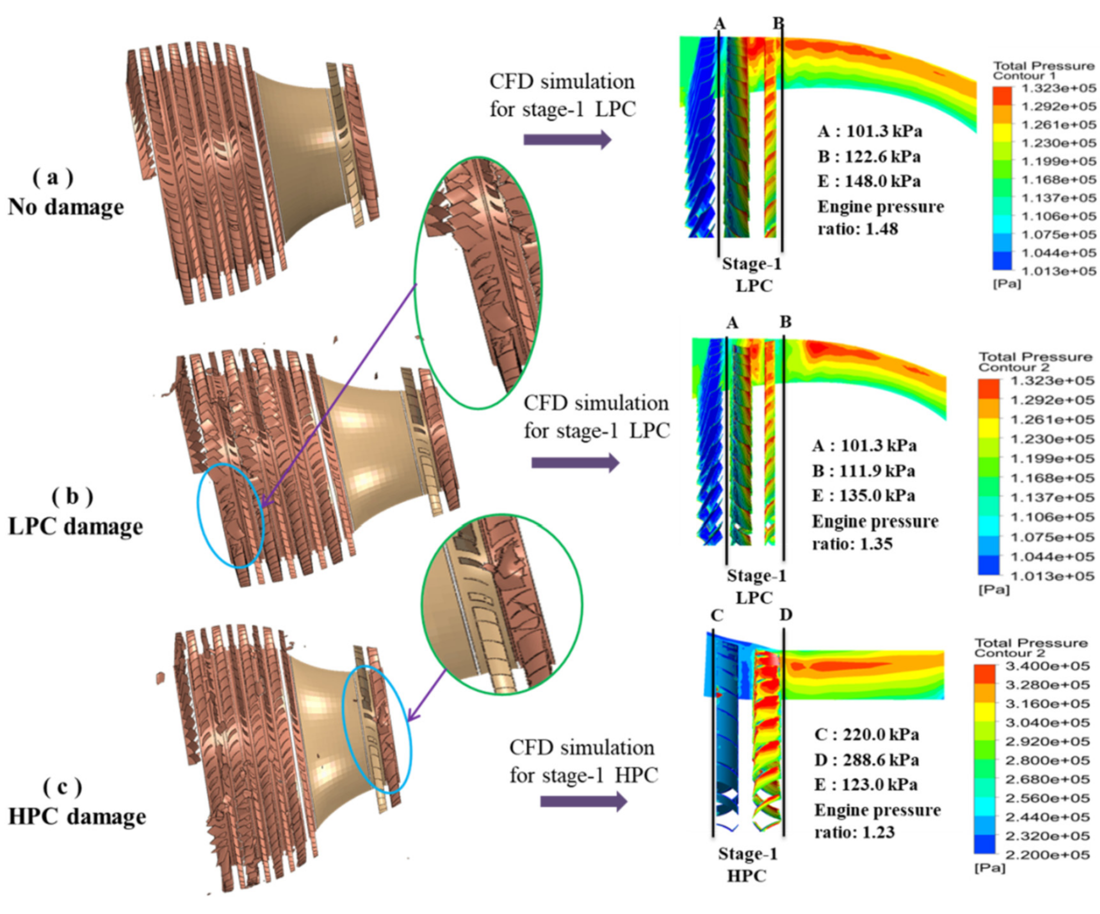

Fig. 21. Total pressure in the damaged stage of compressor core for different collision positions under approach flight phase: (a) no damaged stage-1 LPC (collision position 75%), (b) damaged stage-1 LPC (collision position 25%), (c) damaged stage-1 HPC (collision position 12.5%).

This paper is a primary attempt to simulate the collision severity and resultant thrust loss of engine caused by UAV airborne collision, and only one type of drone is considered. More studies on the aircraft engine subjected to the strike of UAV with different categories [10] can be further performed to build the risk matrix of UAV airborne collision [62][63] in the future work. Vibration study and frequency analysis [64][65] of the rotating fan blades damaged [66] by the drone impact can also be relevant and useful to areas of airworthiness for drone operations.

Declaration of competing interest

The authors declare that they have no known competing financial interests or personal relationships that could have appeared to influence the work reported in this paper.

Acknowledgements

This research is supported by the Civil Aviation Authority of Singapore and the Nanyang Technological University, Singapore un-

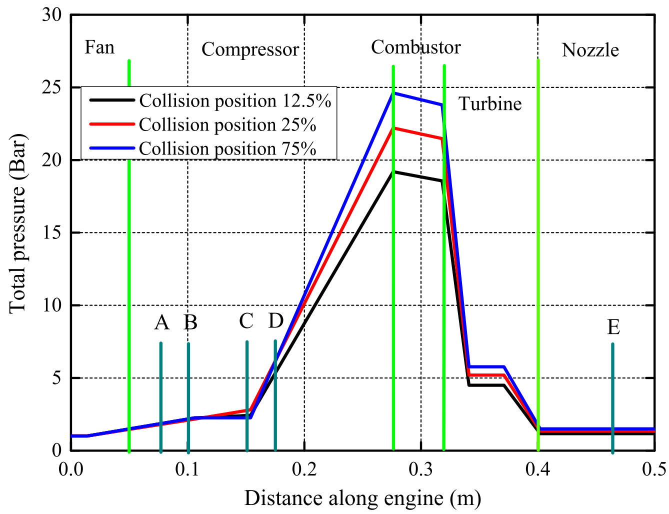

Fig. 22. Total pressure along the aircraft engine for different collision positions under approach flight phase (Labeling A, B, C, D, and E are referred to the positions shown in Fig. 4).

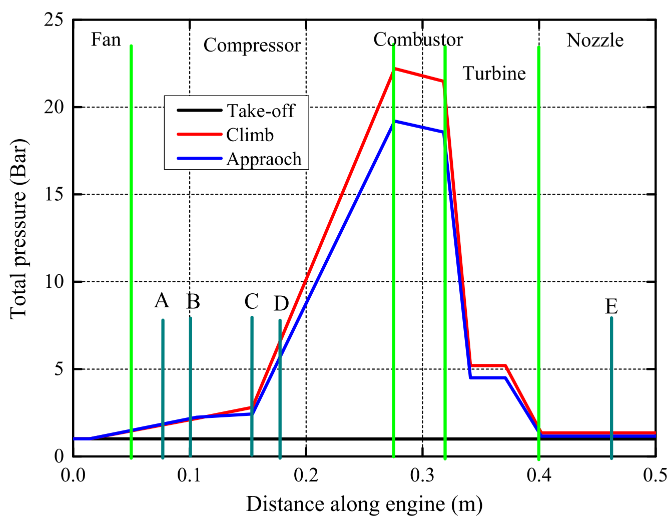

Fig. 23. Total pressure along the engine under different flight phases for collision position of 12.5% (Labeling A, B, C, D, and E are referred to the positions shown in Fig. 4).

der their collaboration in the Air Traffic Management Research Institute. Any opinions, findings and conclusions or recommendations expressed in this material are those of the authors and do not reflect the views of the Civil Aviation Authority of Singapore.

References

[1] Y. Liu, H. Liu, Y. Tian, C. Sun, Reinforcement learning based two-level control framework of UAV swarm for cooperative persistent surveillance in an unknown urban area, Aerosp. Sci. Technol. 98 (2020) 105671.
[2] Z. Zhen, Y. Chen, L. Wen, B. Han, An intelligent cooperative mission planning scheme of UAV swarm in uncertain dynamic environment, Aerosp. Sci. Technol. 100 (2020) 105826.
[3] K. Eliker, S. Grouni, M. Tadjine, W. Zhang, Practical finite time adaptive robust flight control system for quad-copter UAVs, Aerosp. Sci. Technol. 98 (2020) 105708.
[4] D. Jenkins, B. Vasigh, The economic impact of unmanned aircraft systems integration in the United States: Association for Unmanned Vehicle Systems International (AUVSI), 2013.
[5] C.H.J. Wang, S.K. Tan, K.H. Low, Three-dimensional (3D) Monte-Carlo modeling for UAS collision risk management in restricted airport airspace, Aerosp. Sci. Technol. 105 (2020) 105964.
[6] Airprox involving UAS Drones Database, https://www.airproxboard.org.uk/Reports-and-analysis/Statistics/Airprox-involving-UAS-Drones/.
[7] N. Zhang, H. Liu, B.F. Ng, K.H. Low, Collision probability between intruding drone and commercial aircraft in airport restricted area based on collision-course trajectory planning, Transp. Res., Part C, Emerg. Technol. 120 (2020) 102736.
[8] G. Olivares, L. Gomez, J. Espinosa de los Monteros, R.J. Baldridge, C. Zinzuwadia, T. Aldag, Volume II–UAS Airborne Collision Severity Evaluation–Quadcopter, 2017.
[9] G. Olivares, T. Lacy, L. Gomez, J. Espinosa de los Monteros, R.J. Baldridge, C. Zinzuwadia, et al., Volume III–UAS Airborne Collision Severity Evaluation–Fixed-Wing, 2017.
[10] X. Lu, X. Liu, Y. Li, Y. Zhang, H. Zuo, Simulations of airborne collisions between drones and an aircraft windshield, Aerosp. Sci. Technol. 98 (2020) 105713.
[11] X. Meng, Y. Sun, J. Yu, Z. Tang, J. Liu, T. Suo, et al., Dynamic response of the horizontal stabilizer during UAS airborne collision, Int. J. Impact Eng. 126 (2019) 50–61.
[12] K. D'Souza, T. Lyons, T. Lacy, K.R. Kota, Volume IV–UAS Airborne Collision Severity Evaluation–Engine Ingestion, 2017.
[13] Y. Song, B. Horton, J. Bayandor, Investigation of UAS ingestion into high-bypass engines, Part 1: bird vs. drone, in: 58th AIAA/ASCE/AHS/ASC Structures, Structural Dynamics, and Materials Conference, 2017, p. 0186.
[14] K. Schroeder, Y. Song, B. Horton, J. Bayandor, Investigation of UAS ingestion into high-bypass engines, Part 2: parametric drone study, in: 58th AIAA/ASCE/AHS/ASC Structures, Structural Dynamics, and Materials Conference, 2017, p. 0187.
[15] T. Lyons, K. D'Souza, Parametric study of a unmanned aerial vehicle ingestion into a business jet size fan assembly model, J. Eng. Gas Turbines Power 141 (2019) 071002.
[16] H. Liu, H.C.M. Mohd, B.F. Ng, K.H. Low, Airborne collision evaluation between drone and aircraft engine: effects of position and posture on damage of fan blades, in: AIAA Aviation 2020 Forum, 2020.
[17] J. Pernas-Sánchez, J. Artero-Guerrero, D. Varas, J. Lopez-Puente, Artificial bird strike on Hopkinson tube device: experimental and numerical analysis, Int. J. Impact Eng. (2019) 103477.
[18] A. Riccio, R. Cristiano, S. Saputo, A. Sellitto, Numerical methodologies for simulating bird-strike on composite wings, Compos. Struct. 202 (2018) 590–602.
[19] M.L. Cerquaglia, G. Deliége, R. Boman, L. Papeleux, J.P. Ponthot, Reprint of: the particle finite element method for the numerical simulation of bird strike, Int. J. Impact Eng. 110 (2017) 72–84.
[20] I.C. Metz, J. Ellerbroek, T. Mühlhausen, D. Kügler, J.M. Hoekstra, The bird strike challenge, Aerospace 7 (2020) 26.
[21] D-H. Kim, S-W. Kim, Evaluation of bird strike-induced damages of helicopter composite fuel tank assembly based on fluid-structure interaction analysis, Compos. Struct. 210 (2019) 676–686.
[22] S. Heimbs, Computational methods for bird strike simulations: a review, Comput. Struct. 89 (2011) 2093–2112.
[23] R.A. Dolbeer, S.E. Wright, J. Weller, A.L. Anderson, M.J. Begier, Wildlife strikes to civil aircraft in the United States 1990-2014, 2015.
[24] Z. Yu, P. Xue, P. Yao, M.S. Zahran, Analytical determination of the critical impact location for wing leading edge under birdstrike, Lat. Am. J. Solids Struct. 16 (2019) e152.
[25] F. Di Caprio, D. Cristillo, S. Saputo, M. Guida, A. Riccio, Crashworthiness of wing leading edges under bird impact event, Compos. Struct. 216 (2019) 39–52.
[26] S. Orlando, F. Marulo, M. Guida, F. Timbrato, Bird strike assessment for a composite wing flap, Int. J. Crashworthiness 23 (2017) 219–235.
[27] S. Saputo, A. Sellitto, A. Riccio, F. Di Caprio, Crashworthiness of a composite wing section: numerical investigation of the bird strike phenomenon by using a coupled Eulerian–Lagrangian approach, J. Mater. Eng. Perform. 28 (2019) 3228–3238.
[28] Z. Zhang, L. Li, D. Zhang, Effect of arbitrary yaw/pitch angle in bird strike numerical simulation using SPH method, Aerosp. Sci. Technol. 81 (2018) 284–293.
[29] D. Hu, B. Song, D. Wang, Z. Chen, Experiment and numerical simulation of a full-scale helicopter composite cockpit structure subject to a bird strike, Compos. Struct. 149 (2016) 385–397.
[30] U.A. Dar, M. Awais, H.H. Mian, M.Z. Sheikh, The effect of representative bird model and its impact direction on crashworthiness of aircraft windshield and canopy structure, Proc. Inst. Mech. Eng., G J. Aerosp. Eng. 233 (2019) 5150–5163.
[31] FAA Wildlife Strike Database, https://wildlife.faa.gov/search.
[32] S. Meguid, R. Mao, T. Ng, FE analysis of geometry effects of an artificial bird striking an aeroengine fan blade, Int. J. Impact Eng. 35 (2008) 487–498.
[33] R. Vignjevic, M. Orłowski, T. De Vuyst, J.C. Campbell, A parametric study of bird strike on engine blades, Int. J. Impact Eng. 60 (2013) 44–57.
[34] D. Zhang, Q. Fei, Effect of bird geometry and impact orientation in bird striking on a rotary jet-engine fan analysis using SPH method, Aerosp. Sci. Technol. 54 (2016) 320–329.
[35] J. Liu, D. Zhong, Y. Li, Z. Tang, X. Gao, Z. Zhang, et al., Numerical simulation and test on damage of rotary engine blades impacted by bird, Int. J. Crashworthiness 24 (2018) 106–120.

[36] N. Hou, Y. Li, J. Liu, Numerical simulation of bird impact on hollow blades of titanium fan assembly, J. Aerosp. Eng. 32 (2019) 04019044.
[37] Y. Zhou, Y. Sun, W. Cai, Bird-striking damage of rotating laminates using SPH-CDM method, Aerosp. Sci. Technol. 84 (2019) 265–272.
[38] Y. Zhou, Y. Sun, T. Huang, Impact responses of slender composite plates for bird-strike testing of fan blades, Lat. Am. J. Solids Struct. 16 (2019) 1–12.
[39] L. Liu, G. Luo, W. Chen, Z. Zhao, X. Huang, Dynamic behavior and damage mechanism of 3D braided composite fan blade under bird impact, Int. J. Aerosp. Eng. 2018 (2018) 5906078.
[40] Agency EUAS. Certification specifications and acceptable means of compliance for engines CS-E amendment 5, December 2018.
[41] Administration FA, 14 CFR Part 33 Airworthiness Standards; Engine Bird Ingestion; Final Rule, October 2007.
[42] International C, Training manual CFM56-5B basic engine (Report No.: CTC-063 Level 3), 2000.
[43] Glenn Research Center (NASA), Pressure variation - EPR, Retrieved January 2, 2015, https://www.grc.nasa.gov/WWW/k-12/airplane/epr.html.
[44] M. Saari, Thrust measurement for jet transport operation, SAE Transact. 66 (1958) 357–363.
[45] Baptista FMdC. A 0-D off-Design Performance Prediction Model of the CFM56-5B Turbofan Engine. Portugal: Universidade de Lisboa, 2017.
[46] EASA. Bird Strike Damage & Windshield Bird Strike: Final Report. 2009.
[47] EASA. Type-Certificate Datasheet: for AIRBUS A318-A319-A320-A321. 2015(16).
[48] I. Wakefield, C. Dubuque, Exceeding tire speed during takeoff, Boeing's AERO Mag. (2009) 15–17.
[49] FAA. Continuous Descent Final Approach (AC No: 120-108), 2011.
[50] ABAQUS-Explicit, Abaqus, users manual version 6.11, Hibbit, USA: Karlsson and Sorensen Inc., 2011.
[51] Friction Factors Data, https://roymech.org/Useful_Tables/Tribology/co_of_frict.html.
[52] Accident Report, NTSB/AAR-10/03, PB2010-910403. Loss of Thrust in Both Engines After Encountering a Flock of Birds and Subsequent Ditching on the Hudson River US Airways Flight 1549 Airbus A320-214, N106US Weehawken, New Jersey January 15, 2009.
[53] Federal Aviation Administration (FAA) DoDD, National Aeronautics and Space Administration (NASA), Metallic Materials Properties Development and Standardization (MMPDS) Handbook: MMPDS-11. Battelle Memorial Institute 2016, C5-77.
[54] C.W. Kwon, S.E. Cheon, J.M. Song, H.T. Kim, K.B. Kim, C.B. Shin, S.W. Kim, Characteristics of a lithium-polymer battery based on a lithium powder anode, J. Power Sources 93 (1–2) (2001) 145–150.
[55] T. Wang, Q. Qin, M. Wang, W. Yu, J. Wang, J. Zhang, et al., Blast response of geometrically asymmetric metal honeycomb sandwich plate: experimental and theoretical investigations, Int. J. Impact Eng. 105 (2017) 24–38.
[56] Azom, AISI 4340 Alloy Steel (UNS G43400), Sept. 2012.
[57] Z.-Y. Wang, Y. Zhao, G.-W. Ma, Z.-G. He, A numerical study on the high-velocity impact behavior of pressure pipes, J. Zhejiang Univ. Sci. A 17 (2016) 443–453.
[58] X. Yu, C. Li, S. Chang, C. Xuan, L. Peiyuan, Foreign object damage performance and constitutive modeling of titanium alloy blade, Int. J. Aerosp. Eng. (2020) 10.
[59] First Drone vs Plane crash in slow motion/teaser/(HIFLYZONE), https://www.youtube.com/watch?v=id16HadSjBc&list=PLMutvghZEQRDmNm05PWidzRuFK_O4yJ4X&index=2.
[60] Antonov AN-2 specifications, http://www.an2flyers.org/an2specs.html#:~:text=75%25%20Power%20615%20HP%20at%201910%20RPM.
[61] K. Carney, C. Lawrence, D. Carney, Aircraft engine blade-out dynamics, in: Wayne Mindle (Ed.), Seventh International LS-DYNA Users Conference, Livermore CA, USA, vol. 14, Livermore Software Technology Corporation, 2002, pp. 17–26.
[62] EASA Drone Collision Task Force. European Aviation Safety Agency (2016) 1-33.
[63] H. Liu, H.C.M. Mohd, B.F. Ng, K.H. Low, Airborne Collision Severity Study on Engine Ingestion Caused by Harmless-Categorized Drones, AIAA SciTech, 2021.
[64] G.B. Chai, K.H. Low, On the natural frequencies of beams carrying a concentrated mass, J. Sound Vib. 160 (1) (Jan. 1993) 161–166, https://doi.org/10.1006/jsvi.1993.1011.
[65] K.H. Low, On the methods to derive frequency equations of beams carrying multiple masses, Int. J. Mech. Sci. 43 (3) (Mar. 2001) 871–881, https://doi.org/10.1016/S0020-7403(00)00052-7.
[66] K.H. Low, Eigen-analysis of a tip-loaded beam attached to a rotating joint, J. Vib. Acoust. 112 (4) (Oct. 1990) 497–500, https://doi.org/10.1115/1.2930134.